https://doi.org/10.5194/nhess-2022-262
Preprint. Discussion started: 14 February 2023

Natural Hazards and Earth System Sciences
Discussions

Hurricane Irma: an unprecedented event over the last 3700 years? Geomorphological changes and sedimentological record in Codrington Lagoon, Barbuda.

Maude Biguenet[1,2], Eric Chaumillon[1], Pierre Sabatier[2], Antoine Bastien[3], Emeline Geba[1], Fabien Arnaud[2], Thibault Coulombier[1], Nathalie Feuillet[4]

[1]Université de la Rochelle, UMR 7266 LIENSs, Bâtiment Marie Curie, avenue Michel Crépeau, 17042 La Rochelle cedex, France
[2]Université Savoie Mont Blanc, CNRS UMR 5204 EDYTEM, Bâtiment « Pôle Montagne », 5 bd de la mer Caspienne, 73376 Le Bourget du Lac cedex, France
[3]Université de Bordeaux, UMR 5805-CNRS EPOC, Pessac CEDEX, F-33615, France
[4]Institut de Physique du Globe de Paris, Université de Paris, CNRS, 75005 Paris, France

Correspondence to: Maude Biguenet (maudebiguenet.mb@gmail.com)

Abstract

Low-lying coasts and small islands, such as in the Lesser Antilles, are particularly vulnerable to hurricane-induced marine floods. In September 2017, Category 5 Hurricane Irma, with winds up to 360 km/h, hit the northern Caribbean islands and caused the destruction of 95% of the structures on Barbuda Island. We investigated the geomorphological impacts and the sedimentological record of this hurricane in Barbuda's Codrington Lagoon. Following Hurricane Irma, two wide inlets developed across the Codrington sandy barrier. One of these inlets enlarged and was still open~~ed~~ four years later. From available data, it seems that this barrier remained continuous for the last 250 years before Hurricane Irma. At a longer time scale, very high-resolution seismic exploration combined with sediment cores sampled in Codrington Lagoon were used to investigate the Irma deposit and environmental changes for the last 3700 years. The evolution from a low-energy small and shallow lagoon to the modern wide and high-energy lagoon recorded by the lagoon sediment-fill was related to both long-term sea-level rise and subsidence. The top of the lagoon fill consists of a thick and extensive sand sheet recording an abrupt increase in energy. Given its location at the top of the cores, its very recent age supported by short-lived radionuclides data, together with large inlets opening and barrier erosion after Irma implying a large sand supply to the lagoon, this sand sheet was attributed to Hurricane Irma. From our cores, it appears that this deposit is unique over more than 3700 years. Both the opening of a new inlet and the thick upper sand sheet support the exceptional character of Irma at the scale of centuries to millennia. Our study reinforces the idea that Hurricane Irma was exceptional in terms of intensity and may be associated with global warming.

1 Introduction

Hurricanes ~~storms~~ represent a direct threat to coastal territories and populations. Indeed, they generate wind exposure, spin-up tornados, tropical rainfall, storm surge and wind waves. These may cause widespread power outages, coastal and inland flooding, beach erosion, infrastructure and structural damage, and direct human deaths (e.g., Gerritsen, 2005; Griffis, 2007; Karim and Mimura, 2008; Breilh et al., 2013; Takagi et al., 2017; Bacopoulos, 2019). Many studies have reported a notable increase in hurricane intensity and associated damages over recent decades (e.g., Kossin et al., 2013; Holland and Bruyère, 2014; Knutson et al., 2019; Kossin et al., 2020). Pfleiderer et al. (2022) recently showed that the increase in Atlantic tropical cyclone activity since the 1980s can be robustly ascribed to variations in atmospheric circulation as well as sea surface

https://doi.org/10.5194/nhess-2022-262
Preprint. Discussion started: 14 February 2023

Natural Hazards and Earth System Sciences
Discussions

temperature (SST) rise. They found that the forced warming trend in Atlantic SSTs over the 1982–2020 period doubled the probability of extremely active tropical cyclone seasons. Given the projected increases in SSTs with increasing warming, this suggests that the probability of extreme seasons (with category 4-5 hurricanes) might further be more regular in the future. These high category hurricanes generate very high intensity winds that can allow the development of strong surges, leading to large coastal flooding. Thus, low-lying coasts and islands are particularly vulnerable to hurricane-induced submersion. Consequently, the sea level rise associated with the increase in hurricane intensity exposes a growing number of them to marine submersion (Bhatia et al., 2019; Pfleiderer et al., 2022). The question for local communities is hence no more « if » they will be hit by an impacting hurricane, but « when » and even more « in what extent » and "with which consequences" on both natural geomorphic defenses and man-made infrastructures. Thus, it is crucial to understand the coastline geomorphological and sedimentological changes in response to hurricane processes to better inform and prepare coastal communities. (Spiske et al., 2021).

On August 30, 2017, a tropical storm developed west of the Cape Verde Islands (Cangialosi, et al., 2018). It was generated by the combination of warm ocean surface temperatures (30–32 °C) and little atmospheric shear (Bacopoulos, 2019). The tropical storm transitioned to a category 5 hurricane on the 5th of September and was named Irma. Hurricane Irma broke meteorological-based records for tropical cyclones in the Atlantic basin (Cangialosi et al., 2018). It was the strongest hurricane to form in the Atlantic Ocean in historical times, outside of the Gulf of Mexico and the Caribbean Sea (Cangialosi et al., 2018). It remained a category 5 hurricane for 3 days, which is the longest category 5 hurricane since satellite storm tracking began (Bacopoulos, 2019). Furthermore, hurricane winds were maintained for a total of 37 h at 185 mph (298 km hr^{-1}), which is the longest period of such intensity (maximum sustained winds) among all storms on record (Bacopoulos, 2019). Irma made seven landfalls through the following days, four of which occurred as a category 5 hurricane across the northern Caribbean islands (Barbuda, Saint-Martin, Virgin Gorda in the British Virgin Islands and Cayo Romano in Cuba) (Cangialosi et al., 2018). Hurricane Irma brought many coastal hazards such as wind exposure, spin-up tornados, tropical rainfall, storm surge, and wind waves. The consequences included widespread power outages, coastal and inland flooding, beach erosion, infrastructure and other structural damages, and 47 direct human deaths (Bacopoulos, 2019). Damages have costed record-breaking totals, with amounts reaching approximately $51 billion USD for the USA (Bacopoulos, 2019), and $3170 million USD for the Lesser Antilles, the Turks and the Caicos Islands and Cuba. The costs reached $150 to 300 million USD for Barbuda Island alone (Cangialosi et al., 2018). The eye of the storm storm's eye passed directly through Barbuda Island, exposing the island at its peak intensity with a mean wind speed of 155 kt (287 km/h), maximum recorded gusts of wind speed of 360 km/h, and a minimum pressure of 914 mb for more than three hours. Irma's catastrophic winds caused destruction across the island, damaging or destroying approximately 95% of the structures and causing the direct death of three people (Cangialosi et al., 2018). The damages to housing and infrastructure were so extensive that all 1800 residents of the island were immediately evacuated post- hurricane to the neighboring island of Antigua (Boger et al., 2020). This decision was made due to the threat posed by the category 4 hurricane Jose, which passed 60 km north of the island on September 8 (Berg, 2018).

West of Barbuda, Codrington Lagoon and its barrier were strongly hit by Irma and have the potential to record older hurricanes. Thus, they are a key area for showing the impacts of such kind of extreme events. This article aims to document at documenting the impact of Hurricane Irma on the geomorphology and sedimentation of Codrington Barrier and Lagoon. The geomorphological changes of the Codrington Lagoon sandy barrier are examined through recent satellite images, as well as seismic profiles, and compared with older satellite images and nautical maps, allowing a 250-year-long observation of the barrier morphology. Additionally, we sampled six sedimentary cores seven months after the event to document the

https://doi.org/10.5194/nhess-2022-262
Preprint. Discussion started: 14 February 2023


Natural Hazards and Earth System Sciences Discussions

sedimentary record of this extreme event. Furthermore, the study of the complete sedimentary sequences through a multiproxy approach (sedimentological, geochemical, and microfaunal analyses) allowed us to replace this event within a long-term perspective and question its relative importance over the last thousands of years.

2 Study site

2.1 Geomorphologic and geologic setting

Barbuda Island is ~~located~~ in the northeastern part of the Lesser Antilles Arc, 40 km north of Antigua Island (Fig. 1A). These two islands are surrounded by a large and up to 100 m deep carbonate platform called Barbuda Bank (Cornée et al., 2021). Barbuda Island is 13 km wide from east to ~~the~~ west and 22 km long from northwest to southeast (Fig. 1B). The highest point of the island is ~~lying~~ 39 m above mean sea level (a.s.l.) and located in the so-called Highlands area (Weil-Accardo et al., 2022) (Fig. 1B). This low-lying island consists of coral limestone and is almost completely surrounded by fringing and barrier reefs, primarily along its eastern and northern coasts, while the western coast consists of patch reefs. The marine hydrodynamic regime in the island area displays a diurnal microtidal range, which is slightly more than 0.3 m throughout the year (Brasier, 1975a). The island displays a karstic limestone landscape containing numerous sinkholes and caves that retain fresh ~~-~~water throughout the year (Boger et al., 2020) and no surface streams (Potter et al., 2017). A series of saline ponds situated in the southern part of the island (Fig. 1B) are periodically flooded by spring tides and sea water during storms (Potter et al., 2017). The main permanent water body on the island is the hypersaline (measured at approximately 40 ‰ in 1970-1971, Stoddart et al., 1973) Codrington lagoon (Fig. 1B, C, D). This lagoon lies in the western part of the island and is approximately 9 km long and 2.5 km wide. The Codrington Lagoon water depth ranges between 1 and 4.5 m, with a deeper part to the south (as observed in March 2018; Fig. 1C). This lagoon is separated from the ocean to the west by an approximately 1 to 3 m high (as observed in March 2018) and 140 to 260 m wide sandy barrier (Fig. 1C). This barrier is mostly made of coral debris, mollusks, calcareous algae, and foraminifers and hosts a hypersaline sparse vegetation made of herbs and bushes. Prior to Hurricane Irma (September 2017), the barrier was continuous (Fig. 1C), and the northern part of the lagoon was connected to the ocean through a narrow channel, locally called “the creek” (Fig. 1B). After Hurricane Irma, two inlets developed (Fig. 1B, D). The eastern part of the lagoon is fringed by dense mangroves. The only human settlement on the island, Codrington village, is located on the eastern edge of the lagoon (Fig. 1B). The lagoon’s bottom sediment is covered by sea grasses (i.e., Thalassia testudinum, whose root system can reach 80 cm below the sediment surface), algae, and a few scattered coral species (Brasier, 1975a; Glumac and Curran, 2016; Potter et al., 2017).

2.2 Past hurricanes in Barbuda

Barbuda is located within the so-called Atlantic hurricane belt. Therefore, hurricanes are a major and frequent hazard, mostly between June and November (Boger et al., 2020). Many deposits related to past hurricanes were revealed by sedimentary studies along the coasts of various islands, in lagoons and sinkholes in this region (Donnelly and Woodruff, 2007; McCloskey and Keller, 2009; Malaizé et al., 2011; Denommee et al., 2015; Donnelly et al., 2015; Wallace et al., 2019; Biguenet et al., 2021; Winkler et al., 2022). Some paleotempestology studies have been conducted in Barbuda (Knowles, 2008; Burn et al., 2016), but none have been conducted in Codrington Lagoon. Burn et al. (2016) presented a reconstruction of Caribbean effective precipitation during the Little Ice Age, based on the study of the sediment infill of

https://doi.org/10.5194/nhess-2022-262
Preprint. Discussion started: 14 February 2023


Natural Hazards and Earth System Sciences Discussions

one of Barbuda's ponds (Freshwater Pond). Knowles (2008) analyzed transects of sediment cores from another Barbuda's small pond (Salt Pond) and identified overwash deposits and climate variability over the last 5000 years. The oldest historically known hurricane that struck Barbuda Island occurred on 11 September 1813 (Oliver, 1894). The current observational record in the Lesser Antilles began in approximately 1850 CE. Thirteen hurricanes passed within 30 km of Barbuda's Codrington lagoon from 1859 to 2017 according to the National Oceanic and Atmospheric Administration (NOAA) (NOAA, 2021, Historical Hurricane Tracks) (Table 1, Fig. 2). Among the recent hurricanes that struck Barbuda Island, the Category 3 Hurricane Donna in 1960 (Dunn, 1961) and Category 4 Hurricane Luis in 1995 (Hoggarth, 2001) were particularly destructive. Both caused significant damage to houses within Codrington Village (Knowles, 2008). Hurricane Luis even breached a narrow strip of sedimentary barrier across the lagoon that was rapidly filled after the event (Potter et al., 2017). Low Bay beach located to the west of the Codrington Lagoon sandy barrier (Fig. 1B) experienced erosion after this event. The monitoring of this beach between 1996 and 2000 showed that erosion was dominant, with a mean profile area and erosion rate of -0.10 m² and -0.80 m/yr, respectively (James, 2003). The Category 5 Hurricane Irma, which occurred in September 2017, was the latest and strongest hurricane that struck Barbuda (Table 1, Fig. 2). The storm's eye passed directly through Barbuda, exposing the island at its peak intensity with a wind speed of 155 kt (287 km/h) and pressure of 914 mb for more than three hours (Table 1). Irma's catastrophic winds caused destruction across the island, damaging or destroying approximately 95% of the structures and causing the direct death of three people (Cangialosi et al., 2018). The damages to housing and infrastructure were so extensive that all 1800 residents of the island were immediately evacuated to the neighboring island of Antigua after the hurricane (Boger et al., 2020). Hurricane Irma also induced a significant storm surge with a peak water level at 2.4 m mean higher high water (MHHW) recorded at a tide gauge located on Barbuda (Cangialosi et al., 2018). This storm surge induced marine flooding with runup reported to reach some 600 meters inland (United Nations Development Programme, 2019).

2.3 Other possible sources of overwashes in Barbuda: tsunamis

The Lesser Antilles Arc (Fig. 1A) forms the eastern boundary of the Caribbean Plate. This area is characterized by the subduction of the North American Plate under the Caribbean Plate (2 cm yr^{-1}, DeMets et al., 2000). Thus, many active faults and volcanoes lie in the Lesser Antilles Arc and may generate tsunamis. During the historical period, only a few tsunamis were documented in the area (Zahibo and Pelinovsky, 2001; Lander et al., 2002; Harbitz et al., 2012; Engel et al., 2016). The primary sources for tsunamis were earthquakes (local, regional, or far-field) (Reid and Taber, 1920; Pelinovsky et al., 2004; Zahibo et al., 2005; Roger et al., 2011; Harbitz et al., 2012; Cordrie et al., 2019; Biguenet et al., 2021) and volcanic processes (e.g., Pelinovsky et al., 2004; Watt et al., 2012). In the following, we describe major earthquake events and associated tsunamis that occurred locally in the Antigua-Barbuda area, then those that occurred regionally in the northern part of the Lesser Antilles and then far-field events that hit the region. In the Antigua-Barbuda area, the 6 April 1690 CE event is the oldest historically documented tsunami. It reached Antigua, Saint Kitts and Nevis, St. Thomas (U.S. Virgin Islands), and Guadeloupe. This event was generated by an estimated magnitude of Ms 8 earthquake (Robson, 1964; Dorel, 1981; NGDC/WDS, 2020), and the epicenter was probably located between Nevis, Antigua, and Montserrat (Feuillet et al., 2011). On 8 February 1843 CE, a small tsunami (wave amplitude of 1.2 m) was observed in English Harbor at Antigua and Nevis (Shepherd, 1992). The tsunami was generated by a M7.5 to 8 earthquake (depending on the authors) between Antigua and Guadeloupe (Sainte-Claire Deville, 1843; Bernard and Lambert, 1988; Feuillet et al., 2011b; Hough, 2013). More recently (8 October 1974), a large earthquake (Ms = 7.1 to 7.6) occurred near Barbuda, north of Antigua, but did not generate any documented tsunami waves (Mccann et al., 1982). Apart from Barbuda itself, the oldest documented

https://doi.org/10.5194/nhess-2022-262
Preprint. Discussion started: 14 February 2023

Natural Hazards and Earth System Sciences
Discussions

tsunami in the northern part of the Lesser Antilles region is a Pre-Columbian tsunami (dated between 1200 and 1450 years cal. CE from ^{14}C dating). It was identified within sedimentary cores sampled in St-. Thomas (US Virgin Islands; Fuentes et al., 2017), Anegada (British Virgin Islands; Atwater et al., 2017) and Scrub Island (Anguilla; Biguenet et al., 2021). The possible source for this tsunami is a magnitude 9 thrust earthquake located at the subduction interface facing Anegada Island (Cordrie et al., 2022). On 18 November ~~18th~~ 1867, another tsunami was documented in the Virgin Islands and Guadeloupe. This event was probably triggered by a strong earthquake in the British Virgin Islands (Reid and Taber, 1920), but its origin needs to be precisely defined (Zahibo et al., 2003). Finally, a Transoceanic Tsunami was observed in 1755 at 18 locations across the northeastern Caribbean from Bridgetown (Barbados) to Santiago de Cuba (Cuba) (NGDC/WDS, 2020). It was triggered by the well-known Mw 8 to 9 Lisbon earthquake (Chester, 2001).

3 Materials and methods

3.1 Old nautical maps

The morphological evolution of the Codrington Lagoon and its western sandy barrier was studied from a compilation of old nautical maps. The chosen maps were selected according to their date of publication. We cho~~o~~se the oldest known map (1750-1785 CE, Tweedy, 1981), the first accurate and detailed known map (1813 CE, Bain et al., 2018), and then two other maps illustrating the morphology of the island at the end of the 19th (Fullarton et al., 1872) and 20th (Wigley, 1973) centuries. Although other maps of the island exist, they do not show significant morphological changes of the Codrington Lagoon and its western sandy barrier compared to the selected maps.

3.2 Satellite images

The morphological evolution of the western sandy barrier of the Codrington Lagoon over the period 1982–2021 is evidenced from a set of satellite images (Landsat and Global Land Survey data sets). All the images were downloaded from the Global Visualization Viewer of the U.S. Geological Survey website (glovis.usgs.gov). The Global Land Survey (GLS) data sets were created by USGS and NASA using the primary Landsat sensor in use at the time for each collection epoch. The images were chosen according to their dates and the absence of clouds on the western sandy barrier. All the images have been resized to focus on Codrington Lagoon and facilitate the comparisons of the images. Our selection includes (1) three Landsat 1 – 5 images from 1982 to 1992 using Multispectral Scanner (MSS) Level-1 (images processed to a 60 meter pixel size); (2) one GLS2000 image from 1999, which uses Landsat 7 Enhanced Thematic Mapper Plus (ETM+), with a data resolution of 30 meters; (3) two GLS2005 images from 2003 and 2006, which uses a combination of Landsat 7 ETM+ and Landsat 5 TM, with a data resolution of 30 meters; (4) one GLS2010 image from 2010, which uses a combination of Landsat 7 ETM+ and Landsat 5 TM, with a data resolution of 30 meters; and (5) eleven Landsat 8 OLI (Operational Land Imager) images from 2013 to 2021, with 15 to 30 meter resolution.

3.3 Very high-resolution seismic exploration

During June 2021, a seismic survey was carried out within the Codrington Lagoon. A boomer plate associated with a line in a cone receiver, with a vertical resolution of 25 cm (IKB-Seistec, Simpkin and Davis, 1993), was used to image the detailed internal architecture of the lagoon sediment fill. The shot interval was 250 ms, corresponding to an average distance between adjacent seismic traces of 0.125 m for a ship speed of 1 knot. Despite adverse weather conditions (strong winds

https://doi.org/10.5194/nhess-2022-262
Preprint. Discussion started: 14 February 2023

Natural Hazards and Earth System Sciences
Discussions

between 18 and 40 knots and wind waves in the lagoon during the survey), 16 seismic profiles were recorded for a total length of 7131 m. Two seismic profiles displaying the typical internal architecture of the lagoon fill and new inlet are shown (profiles 13 and 15, respectively, Fig. 1D). The locations of the other seismic profiles can be found in the Supplementary section. Seismic data processing was carried out using Delph Seismic Interpretation software, consisting of (1) noise mute in the water column; (2) swell filtering; (3) automatic gain correction; and (4) bandpass filtering. We used a 1500 m.s-1 P-wave velocity for the two-way travel time to depth conversion.

3.4 Sampling and core description

The sampling was carried out in March 2018, using an Uwitec gravity corer with a hammer. Six sediment cores of 60 to 130 cm were sampled in Codrington Lagoon at water depths of 3.2 to 4.5 m. The core locations were chosen along transects perpendicular to the lagoon western sandy barrier. A south transect was conducted in front of the southern inlet (Fig. 1D), including from west to east, cores BARB1-18-01 (n°IGSN TOAE0000000494), BARB1-18-02 (n°IGSN TOAE0000000495) and BARB1-18-03 (n°IGSN TOAE0000000496). A central transect was followed in front of the lagoon central inlet (Fig. 1D), including from west to the east cores BARB1-18-05 (n°IGSN TOAE0000000498) and BARB1-18-06 (n°IGSN TOAE0000000499). Finally, core BARB1-18-09 (n°IGSN TOAE0000000502) was taken just north of the central inlet (Fig. 1D). Cores have been split, described in detail, photographed, and subsampled in the laboratory. The cores were horizontally stored in the laboratory walk-in cooler. Core locations and sampling procedures can be found in the French National Cyber-core repository (https://cybercarotheque.fr/index.php).

3.5 Sedimentological analyses

For this study, sedimentological analyses were conducted on cores BARB1-18-01 and BARB1-18-05. Grain-size analyses were carried out at the EDYTEM laboratory using a Beckman Coulter LS 13320 XR particle size analyzer using sonication, with a range size between 0.010 µm and 3000 µm. The sampling step was approximately 1 cm through cores BARB1-18-01 (n = 132) and BARB1-18-05 (n = 123), respecting facies boundaries. No pretreatment was conducted on the samples. The shells larger than 2 mm were removed from every sample. Because of the~~ir~~ large shell debris content ~~in shells debris~~, the mean grain sizes of sampled sediment were not coherent with the visual observations. Thus, grain-size studies were restricted to particles smaller than 1 mm. The grain-size results were processed using an EMMA algorithm implemented by QGrain software using the machine learning framework PyTorch (Liu et al., 2021). For core BARB1-18-01, an EMMA algorithm with 3 ~~e~~End-~~M~~members was chosen, as it best suited the ~~core~~ main grain-size observations of the core. The sum of the end-members corresponds to 100% of the grain-size frequency per sample. These three end-members correspond to the three main sediment grain-size modes: EM1= 20 µm, EM2= 127 µm and EM3= 269-993 µm. For core BARB1-18-05, the EMMA algorithm that best suited the grain-size observation was the one with 4 ~~e~~End-~~M~~members. These four end-members correspond to the four main sediment grain-size modes: EM1= 4 µm, EM2= 20 and 50 µm, EM3= 127 µm and EM4= 269-623 µm. Given that EM1 and EM2 of core BARB1-18-05 are similar to EM1 of core BARB1-18-01, we ch~~o~~ose to add EM1 and EM2 of core BARB1-18-05. Thus, the grain-size results of cores BARB1-18-05 described and discussed below are EM1= 4-18 µm and 50 µm, EM2= 127 µm, EM3= 269-623.

Core BARB1-18-01 was scanned using an X-ray tomography system (Easytom XL 150 from RX SOLUTION society) at the SYMME laboratory (Annecy, France). The core was cut into two sections (126.5 to 70 cm and 70 to 0 cm). Each section was scanned at 150 kV and 66 µA for approximately 1 h 25 to cover the entire volume of the core (8 successive scans from

https://doi.org/10.5194/nhess-2022-262
Preprint. Discussion started: 14 February 2023

Natural Hazards and Earth System Sciences Discussions

126.5 to 70 cm and 10 successive scans from 70 to 0 cm). The images (16-bit.tif) obtained are cross-sections of the cores (horizontal slices from top to base). For core BARB1-18-01, there were a total of 19-894 (8848 + 11-046) images ~~were~~ available ~~in total for core BARB1-18-01~~. Vertical cross-sections of 63 µm resolution (voxel size) were reconstructed using ImageJ software and including the Fiji distribution extension (Schindelin et al., 2012).

3.6 Geochemical analyses

The six cores were scanned at EDYTEM laboratory using the Avaatech Core Scanner (Avaatech XRF Technology, EDYTEM) with an Rh anode for X-ray fluorescence (XRF) analyses (Richter et al., 2006). For BARB1-18-01, two runs with a 1 mm-step resolution were used to detect light and heavy weight elements: a run at 10 kV and 0.2 mA for 20 s and a run at 30 kV and 0.3 mA for 20 s with three replicates every 53 mm for both runs. For BARB1-18-02, two runs with a 1 mm-step resolution were used: a run at 10 kV, 0.15 mA for 20 s with and a run at 30 kV, 0.2 mA for 20 s with two replicates every 32 mm for both runs. For BARB1-18-03, two runs with a 2 mm-step resolution were used: a run at 10 kV, 0.2 mA for 20 s with two replicates and a run at 30 kV, 0.3 mA for 20 s with two replicates every 22 mm for both runs. For BARB1-18-05, two runs with a 2 mm-step resolution were used: a run at 10 kV and 0.15 mA for 20 s and a run at 30 kV and 0.2 mA for 20 s with two replicates every 32 mm for both runs. For BARB1-18-06, two runs with a 2 mm-step resolution were used: a run at 10 kV and 0.2 mA for 20 s and a run at 30 kV and 0.3 mA for 20 s with three replicates every 43 mm for both runs. For BARB1-18-09, two runs with a 1 mm step were used: a run at 10 kV and 0.1 mA for 20 s and a run at 30 kV and 0.15 mA for 20 s with two replicates every 22 mm for both runs. Element relative abundances were expressed as centered log-ratios (CLRs) to avoid dilution effects due to water~~, for example~~ (e.g., Weltje et al., 2015). These values were calculated using the equation from Weltje et al. (2015).

For core BARB1-18-01, the following elements (n = 12) were used to calculate the geometric mean: Al, Si, S, Cl, K, Ca, Ti, Fe, Ni, Cu, Br, and Sr. Elements Na, Mg, P, Mn, Zn, Rb, Zr and Pb were not used because they display high uncertainties with a very noisy signal. For core BARB1-18-05, the following elements (n = 15) were used to calculate the geometric mean: Na, Mg, Al, Si, Cl, K, Ca, Ti, Mn, Fe, Ni, Cu, Zn, Br and Sr. The elements P, S, Rb, Zr and Pb were not used because of high uncertainties with a very noisy signal.

To highlight chemical endmembers (e.g., Sabatier et al., 2010b) and element correlations, principal component analysis (PCA) was performed on the raw XRF data of core BARB1-18-01 and BARB1-18-05 using software R (R Core Team, 2020).

To quantify the amount of organic matter (LOI550) and carbonates (LOI950) in core BARB1-18-01 and BARB1-18-05, loss on ignition (LOI) analyses were performed following the protocol described by Heiri et al.~~,~~ (2001). The sampling step was 4 cm (n=33 and n=31). Biguenet et al. (2021) showed that for carbonate-rich sediments, the 2 h at 950 °C proposed in the protocol was not sufficient to burn all carbonates. Here, the carbonate content in the samples was 3 to 17% higher after a second burn at 950°C.

Slabs (8.5 × 1.5 cm) were sampled from cores BARB1-18-01 (n=6) and BARB1-18-05 (n=4) to be resin-embedded. The small-scale sedimentary structures and grains of the slabs were observed with a LEO Stereoscan 440 Leica (ASTRE platform of the Université Savoie Mont-Blanc) scanning electron microscope (SEM) with 20 kV tension and at a 10 mm work distance. The elementary composition at the grain scale was highlighted through chemical maps that were performed on the slabs at a 24 mm work distance using the Quantax EDX probe (Bruker) from the ASTRE platform. The images were obtained in high vacuum mode in secondary electron or backscattering electron modes.

https://doi.org/10.5194/nhess-2022-262
Preprint. Discussion started: 14 February 2023

Natural Hazards and Earth System Sciences
Discussions
Open Access
EGU

3.7 Foraminifera analyses

To analyze the sediment foraminifera content, samples were taken every 5 to 10 cm and every 10 cm according to sedimentary facies boundaries in cores BARB1-18-01 (n=20) and BARB1-18-05 (n=13). Samples were weighed and dried at 60 °C. The dried residues were sieved to retain the foraminifera from the 125–500 µm and > 500 µm fractions. Individuals were identified at least at the genus level, using common taxonomical reference literature describing the foraminifera in the Gulf of Mexico and the Caribbean Sea. To determine the foraminifera abundance per sample, a semi-quantitative scale was elaborated, based on the number of specimens observed in a single 6 × 10 cm picking tray filled with dry residue.

3.8 Chronology

Short-lived radionuclides (^{210}Pb, ^{137}Cs) were measured using well-type Ge detectors at the Laboratoire Souterrain de Modane (methods from Reyss et al., 1995). Samples were collected from cores BARB1-18-01 (n=23) and BARB1-18-05 (n=21), in the upper 34 cm and 30 cm respectively, according to lithological variations. The difference between total ^{210}Pb and ^{226}Ra activities was attributed to excess ^{210}Pb ("^{210}Pbex") (Goldberg, 1963). Results were calculated using the package 'serac' in R software (Bruel and Sabatier, 2020). Organic macroremains (wood, leaves, and roots) were collected in the six cores (n=21). ^{14}C measurements were carried out by accelerator mass spectrometry (AMS) at the Laboratoire de Mesure du Carbone 14 (LMC14) ARTEMIS at the CEA (Atomic Energy Commission) Institute at Saclay and at the Poznan Radiocarbon Laboratory. The ^{14}C ages were calibrated at two sigma using the Intcal20 calibration curve (Reimer et al., 2020).

4 Results

4.1 Codrington Lagoon sandy barrier morphological evolution from the 18th century to 2021

The compilation of Barbuda old nautical maps (Fig. 3) argues in favour of relatively few morphological changes throughout the period when compared to today's island coastal geomorphology (Fig. 1B). The oldest known map of the island (1750-1785 CE, Fig. 3A), although poorly respectful of the proportions of the island, displays valuable information about the Codrington Lagoon sandy barrier. The "large pond", which corresponds to the current Codrington lagoon, is completely isolated from the open ocean, ~~with the exception of~~except for the narrow channel located in its north area ("the creek"). The three other maps (1813 CE, Fig. 3B; 1872 CE, Fig. 3C; 1973 CE, Fig. 3D) also display a continuous western sandy barrier.

The detailed morphological evolution of the western barrier can be evidenced since 1982 using satellite images (Fig. 4). The barrier was thin but continuous in 1982 and 1986. The barrier remained continuous in 1990 and 1992, although Hurricane Klaus (H1) struck Barbuda in 1990. The first exploitable satellite image after Hurricanes Luis (H4, 1995) and Bertha (H1, 1996) was obtained in 1999. This image shows that the extreme south of the barrier has widened toward the lagoon side (circled in red on the image), displaying a washover morphology. Nevertheless, no breach is observable. The barrier was still continuous on the 2003 satellite image, although Hurricane Debby (H1) struck Barbuda in 2000. The washover observed in 1999 was still visible in February 2017 and was smaller in August 2017. The first usable satellite image after Hurricane Irma, which struck Barbuda Island in September 2017, is from November 2017. Two inlets are observed: a 1.2 km-wide inlet in the center of the barrier and a 0.5 km-wide inlet in the southern part of the barrier. From

https://doi.org/10.5194/nhess-2022-262
Preprint. Discussion started: 14 February 2023

Natural Hazards and Earth System Sciences
Discussions

March to July 2018 (6 to 10 months after the event), the southernmost inlet was filled by sediment. However, the central inlet has enlarged since its formation in 2017 (1.9 km wide in September 2021).

A very high-resolution seismic profile, recorded in June 2021 within the large central inlet opened after Hurricane Irma, allows ~~to~~ the evidence of morphological changes in cross section (Profile 15, Fig. 5). This profile displays two main unconformities (Fig. 5). The basal unconformity EU0 (in green, Fig. 5B) corresponds to an irregular, subhorizontal erosional surface, clearly evidenced by the truncation of underlying reflectors. The upper unconformity EUi (in pink, Fig. 5B) is subhorizontal and less irregular than EU0. EUi is evidenced by downlaps of the overlying reflectors, whereas erosional truncations of underlying reflectors are weakly expressed. The basal unit U0, which lies under EU0, displays a medium amplitude, low continuity and medium frequency reflectors (Fig. 5B). Some reflectors within U0 are subhorizontal to gently inclined. Most of this unit is chaotic to transparent. The low penetration of acoustic waves prevents detailed observations within U0. The outer shape of seismic Ui1, i.e., lying between EU0 and EUi, is a sheet drape with thicknesses ranging from 0.7 to 1.8 m (Fig. 5B). It displays low amplitude, medium continuity and medium frequency reflectors. The reflectors in Ui1 are mostly subhorizontal and gently inclined toward the lagoon in the middle part of the profile. The outer shape of the uppermost unit Ui2 consists of a 1-m-thick sheet drape to the east and to a bank to the west (Fig. 5B). The maximum bank thickness reaches more than 2.5 m. It displays medium to strong amplitude, good continuity, and medium to low frequency reflectors. Reflectors within the eastern part (i.e., lagoonward) of Ui2 are subhorizontal, whereas they are mounded within the western part (i.e., oceanward) of Ui2.

4.2 Sedimentary record in Codrington Lagoon

4.2.1 Seismic stratigraphy of Codrington lagoon

The internal architecture of Codrington Lagoon is illustrated by seismic Profile 13 (Fig. 6), in which three main unconformities are observable. The lowest one, EU0 (in green, Fig. 6B), corresponds to an irregular, subhorizontal erosional surface, clearly evidenced by the truncation of underlying reflectors. The middle unconformity EUl1 is subhorizontal to gently inclined toward the west (in blue, Fig. 6B). This is evidenced by downlapping of the overlying reflectors. The upper unconformity EUl2 is subhorizontal (in orange, Fig. 6B). This is evidenced by toplaps of the underlying reflectors. The basal unit U0 lying under EU0 displays a medium amplitude, medium continuity and medium frequency reflectors (Fig. 6B). Reflectors within U0 are subhorizontal. The outer shape of seismic Ul1 lying between EU0 and EUl1 is a sheet drape with thicknesses ranging from 0.6 to 2 m (Fig. 6B). One strong amplitude reflector, gently inclined to the west, is observed within Ul1. Seismic unit Ul2, which lies between EUl1 and EUl2, displays low to medium amplitude and medium continuity reflectors (Fig. 6B). These reflectors dip to the west and display a shingled internal configuration. Seismic unit Ul3, lying on EUl2, displays medium amplitude and subhorizontal reflectors, with good continuity in the western part of the profile (Fig. 6B). To the east, Ul3 displays low amplitude chaotic reflections. The sea bottom is marked by 3 parallel reflectors that likely correspond to an artifact, as they are frequently observed in very shallow exploration on sandy bottoms (Chaumillon et al., 2008). Seismic profile 13 was set to cross the position of three sediment cores taken in 2018: BARB1-18-01, 02 and 03 (Fig 6). This allowed us to sample sediments within the Ul3 seismic unit. BARB1-18-02 reached the top Ul2 seismic unit below Ul3.

https://doi.org/10.5194/nhess-2022-262
Preprint. Discussion started: 14 February 2023

Natural Hazards and Earth System Sciences
Discussions

4.2.2 Sediment core lithological description

Three main sedimentary facies are distinguishable from the six cores sampled in the Codrington Lagoon. These facies are all included in seismic unit Ul3 (Fig. 6B). Only core BARB1-18-02 may have reached underlying unit Ul2. In the following, sedimentary facies are mainly described from cores BARB1-18-01 and BARB1-18-05.

Facies 1 (F1) consists of light gray to light olive gray fine sand deposited at the top of the six cores (Figs. 7 and 8). F1 thickness varies from 7 to 27 cm in cores BARB1-18-03 and BARB1-18-01, respectively, and becomes thinner with increasing distance from the sandy barrier (Fig. 8). A medium sand F1 layer is also visible in core BARB1-18-09 from 45 to 33 cm depth (Fig. 8). F1 is also observed within five thin layers at the bottom of cores BARB1-18-01 and BARB1-18-02 (0.25- to 4-cm-thick) intercalated with Facies 3 (see below). The core BARB1-18-01 X-ray tomography scan highlights these denser layers of fine sand (lighter gray, Fig. 9A). The two deepest layers in core BARB1-18-01 were correlated to two layers in core BARB1-18-02 (Fig. 8). F1 layers are generally characterized by basal sharp contact with the underlying facies. Grain-size endmember analyses of F1 within core BARB1-18-01 show a mean repartition of 24% for EM1 (20 µm), 49% for EM2 (127 µm) and 27% for EM3 (269-993 µm) (Fig. 9A). Grain-size endmembers of F1 within core BARB1-18-05 show a mean repartition of 31% for EM1 (4-18 and 50 µm), 46% for EM2 (127 µm) and 23% for EM3 (269-623 µm) (Fig. 10A). Thus, fine sand EM2 (127 µm) is the main grain-size mode observed in F1. F1 consists of 36.5 (±2.5) % carbonates (LOI950) and 8.5 (±2) % organic matter (LOI550) in cores BARB1-18-01 and BARB1-18-05 (Figs. 9A and 10A). F1 is made of carbonated sand~~. The sand~~, which originates from various eroded fragments of marine skeletal material (e.g., corals, mollusks, bivalves, and foraminifers). Many shell~~s~~ fragments of variable sizes (100 to 1000 µm) are usually mixed with the sand and sometimes form a broken shell layer at the top of the F1 deposit (e.g., cores BARB1-18-05 and BARB1-~~-~~18-06, Fig. 8). The ~~F1 deposits~~ carbonated grains in the F1 deposits (sand grains and shell fragments) are composed of calcite and magnesium calcite (Fig. 7). F1 displays the highest foraminifera diversity in cores BARB1-18-01 and BARB1-18-05, with 14 to 25 different species identified per sample. This rich and intact fauna is dominated by abundant individuals (6 to more than 41 individuals per species in samples from the semiquantitative abundance study) of the symbiont-bearing taxon *Archaias angulatus,* the Miliola sandy taxon *Pseudotriloculina rotunda* and many *Quinqueloculina* species. The robust shaped *Archaias angulatus* is known to live in coarse sand, both inside the Codrington Lagoon and from the shore zone to the fore-reef around the island (Brasier, 1975b). *Pseudotriloculina rotunda* is a sessile and encrusting taxon that thrives near dense vegetation, such as *Thalassia testudinum,* both inside the lagoon and in reefs around Barbuda (Brasier, 1975a, 1975b). Among the many species found in F1, some were restricted to this facies. These rare (1 to 2 individuals per species in samples), very slightly damaged individuals, were found in samples from the F1 layer deposited at the top of BARB1-~~-~~18-01 and BARB1-18-05. These individuals form part of unidentified species, such as *Pyrgo* sp. 1, *Elphidium* sp. 1, *Bolivina* sp. 1 *and Amphistegina* sp. but also *Asterigerina carinata*, *Pseudohauerinella occidentalis, Textularia agglutinans*, *Cymbaloporetta squammosa* and *Monalysidium acicularis*. *A. carinata* (Fig. 7) is known to live outside of the Codrington Lagoon in vegetated bottoms of the marine area west of the present-day sandy barrier (Brasier, 1975b). *P. occidentalis* is found in tropical backreef and reef environments (Javaux and Scott, 2003). *T. agglutinans* (Fig. 7) is known to live in the fore-reef around Barbuda Island (Brasier, 1975b). *C. squammosa* is a sessile and encrusting taxon~~a~~ that lives in vegetated areas of the reef and interreef around Barbuda Island (Brasier, 1975b). *M. acicularis* (Fig. 7) is known to live abundantly in the high intertidal area of Shuaiba Lagoon (eastern Red Sea, Abu-Zied and Bantan, 2013).

https://doi.org/10.5194/nhess-2022-262
Preprint. Discussion started: 14 February 2023


Natural Hazards and Earth System Sciences
Discussions

Facies 2 (F2) is divided into two alternating subfacies: Facies 2A (F2A) and Facies 2B (F2B) (Figs. 7 and 8). The depths and thicknesses of these subfacies vary between cores, revealing lateral facies variations in the lagoon (Fig. 8). F2A consists of light gray to grayish brown sandy silt, with thicknesses varying from 16 to 86 cm in BARB1-18-06 and BARB1-18-02, respectively (Figs. 7 and 8). Grain-size endmembers of F2A within core BARB1-18-01 show a mean repartition of 55% for EM1 (20 µm), 25% for EM2 (127 µm) and 20% for EM3 (269-993 µm) (Fig. 9A). Grain-size endmembers of F2A within core BARB1-18-05 show a mean repartition of 30% for EM1 (4-18 and 50 µm), 34% for EM2 (127 µm) and 36% for EM3 (269-623 µm) (Fig. 10A). Thus, silt with EM1 (20 µm) is the grain-size mode that describes F2A the best for core BARB1-18-01. The three grain-size endmembers of core BARB1-18-05 display almost equivalent percentages, showing a mix of the three main grain-size populations, with the highest percentage being EM3 (269-623 µm). F2A consists of 36.5 (±1.5) % carbonates (LOI950) and 8 (±1.5) % organic matter (LOI550) in cores BARB1-18-01 and BARB1-18-05 (Figs. 9A and 10A). F2A consists of a mix of silt and carbonated sand. The sand originates from various eroded fragments of marine skeletal material (e.g., corals, mollusks, bivalves, and foraminifers). Many shells fragments of variable sizes (100 µm to several centimeters) are usually mixed with the sand. ~~The carbonated~~Carbonated grains contain more or less Mg-rich calcite (Fig. 7).

F2B consists of gray sandy silt, with thicknesses varying from 5 to 30 cm in BARB1-18-09 and BARB1-18-06, respectively (Figs. 7 and 8). This facies is absent from cores BARB1-18-02 and BARB1-18-03. Grain-size endmembers of F2B within core BARB1-18-01 show a mean repartition of 81% for EM1 (20 µm), 11% for EM2 (127 µm) and 8% for EM3 (269-993 µm) (Fig. 9A). Grain-size endmembers of F2B within core BARB1-18-05 show a mean repartition of 52% for EM1 (4-18 and 50 µm), 30% for EM2 (127 µm) and 18% for EM3 (269-623 µm) (Fig. 10A). Thus, silt with EM1 is the grain-size mode that describes F2B the best for both cores, with a higher percentage in core BARB1-18-01, as seen in F2A. F2B consists of 28 (±4) % carbonates (LOI950) and 15 (±3) % organic matter (LOI550) in cores BARB1 -18-01 and BARB1-18-05 (Figs. 9A and 10A). It is mainly composed of a silty Mg-rich-calcite matrix with almost undamaged shells of variable sizes (100 µm to several centimeters) (Fig. 7). The carbonated grains (sand grains and shells) are made of calcite (Fig. 7). F2A and F2B both display 5 to 18 different foraminifera species per sample in cores BARB1-18-01 and BARB1-18-05. This fauna is also dominated by abundant individuals (6 to more than 41 individuals per species in samples) of *A. angulatus, P. rotunda* and many *Quinqueloculina* species. Furthermore, F2A and F2B display many whole and intact bivalve and gastropod shells, with the shells from F2A showing more wear. These shells are of variable sizes (1 to 5 cm) (Fig. 7). The identified individuals found in the sediment were *Bulla striata, Cerithium eburneum, Chione cancellata* and *Tellina sybaritica,* which are known to live in Codrington Lagoon (Brasier and Donahue, 1985).

Facies 3 (F3) consists of gray to light olive gray clay to silt, located at the core bases with a thickness varying from 16 to 47 cm in cores BARB1-18-06 and BARB1-18-05, respectively (Figs. 7 and 8). The transition between F3 ~~Facies 3~~ and F2~~Facies 2~~ in cores BARB1-18-01 and BARB1-18-02 is correlated with the strong amplitude reflector in UI3 (in red, seismic profile 13, Fig. 6B) in unit UI3. F~~acies~~ 3 is absent from the shorter cores BARB1-18-03 and BARB1-18-09. Grain-size endmembers of F3 within core BARB1-18-01 show a mean repartition of 92% for EM1 (20 µm), 7% for EM2 (127 µm) and 1% for EM3 (269-993 µm) (Fig. 9A). Grain-size endmembers of F3 within core BARB1-18-05 show a mean repartition of 97% for EM1 (4-18 and 50 µm), 2% for EM2 (127 µm) and 1% for EM3 (269-623 µm) (Fig. 10A). Thus, F3 is almost exclusively composed of sediment from fine sediment (EM1) for both cores, varying between 4-18 and 50 µm, from clay to silt. The slightly highest percentage of EM2 (127 µm) in core BARB1-18-01 can be explained by the presence of thin F1 layers at its base. F3 is very homogenous with almost nothing apart from the clay to silt matrix. It is composed of 14

https://doi.org/10.5194/nhess-2022-262
Preprint. Discussion started: 14 February 2023


Natural Hazards and Earth System Sciences
Discussions

(±6) % carbonates (LOI950) and 19 (±8) % organic matter (LOI550) in cores BARB1-18-01 and BARB1-18-05 (Figs. 9A and 10A). There were ~~Z~~zero to 11 different foraminifera species ~~were~~ identified per sample in F3 from cores BARB1-18-01 and BARB1-18-05. F~~acies~~ 3 is dominated by many Quinqueloculina species (1 to 15 individuals per species in samples).

4.2.3 Geochemistry

BARB1-18-01 XRF core scanning main results are ~~showed~~ shown in Fig. 9. A moderate relationship is shown between Sr linear regression tests and LOI950 results, with an R value of 0.45 and p value < 0.00003853. These two indicators present the same long-term variation, but this weak relation probably indicates a variable source of Sr, usually found in carbonated shells of micro- and macrofauna. A significant relationship is shown between Br linear regression tests and LOI550 results, with an R value of 0.86 and p value <5.439e-15. As Br is known to have a strong affinity for organic matter (e.g., Chagué-~~-~~Goff and Fyfe, 1996; Bajard et al., 2016; Biguenet et al., 2021), this suggests that Br (CLR) can be used as a high-resolution proxy for organic matter content. F3 simultaneously displays relatively low Sr (CLR) values and high Br (CLR) values, indicating a decrease in carbonate and an increase in organic matter contents (Fig. 10A). F3 also displayed the highest value for Ti (CLR) (Fig. 9A).

The total variance is represented at 85% by the first two dimensions (Dim1 and Dim2) of the PCA (Fig. 9B). Al, Si, K, Ti, Fe and Br show a positive loading on Dim1. Sr and Ca demonstrate a low negative loading on Dim1. Fe and Br (negative loading) can be distinguished from Al, Si, K, and Ti (positive loading) on Dim2. Sr and Ca also show a high positive loading on Dim2, displaying a negative correlation with Br. This PCA representation allows us to identify three different geochemical endmembers: (1) “carbonates” elements illustrated by Ca and Sr; (2) “organic matter” -related elements (OM) represented by Br; and (3) “silicates” allochthonous inputs, represented by Al, Si, K, Fe and Ti. A map of the geochemical data distribution was established from labelling samples with the facies information in the PCA (Fig. 9C). F1 is controlled by the “carbonates” endmember because of the numerous shell fragments with high concentration in Sr and Ca in this facies (e.g., Sabatier et al., 2010b; Chagué-Goff et al., 2017; Biguenet et al., 2021). F2A is also influenced by the “carbonates” endmember with a negative loading on Dim1. F2B seems to be correlated with the “silicates” endmember, while F3 is more influenced by the “organic matter” and to a lesser extent by the “silicates” endmember.

BARB1-18-05 XRF core scanning main results are ~~showed~~ shown in Fig. 10. A highly significant relationship is shown between Sr linear regression tests and LOI950 results, with an R value of ~~of~~ 0.86 and p value < 2.761e-14. Given that Sr is mostly found in carbonated shells of micro- and macrofauna, its variations could be used as high-resolution proxy of carbonated fauna content in the sediment. A weaker relationship compared to core BARB1-18-01 is shown between Br linear regression tests and LOI550 results, with an R value of 0.43 and p value < 0.00004188. The lower LOI550 values (<20%, Fig. 10A) of core BARB1-18-05 may explain the weaker relationship between Br and LOI550 compared to core BARB1- 18-01. F3 displayed the highest value for Ti (CLR) (Fig. 10A).

The total variance is represented at 87% by the first two dimensions (Dim1 and Dim2) of the PCA (Fig. 10B). Cl, Na, Mg, Mn, Fe, K, Ti, Al and Si show a positive loading on Dim1. Ca, Sr and Br have a negative loading on Dim1. Br, Na, Cl, Mg and Mn demonstrate a positive loading on Dim2. Ca, Sr, Fe, K, Ti, Al and Si display a negative loading on Dim2. This PCA representation allows us to identify four different geochemical endmembers: (1) “carbonates” illustrated by Ca and Sr; (2) “organic matter” (OM) represented by Br; (3) “evaporites” represented by Na, Cl, Mg; and (4) “silicates” represented by Fe, K, Ti, Al and Si. A map of the geochemical data distribution was established from labelling samples with the facies information in the PCA (Fig. 10C). F1 and F2A are strongly linked to the “carbonates” endmember. F2B is dominated by

https://doi.org/10.5194/nhess-2022-262
Preprint. Discussion started: 14 February 2023


Natural Hazards and Earth System Sciences Discussions

the "organic matter" endmember and not by the "silicates" endmember, as for core BARB1-18-01. F3 is influenced by both the "evaporites" and "silicates" endmembers, as for core BARB1-18-01.

Thus, it appears that F1 and F2A are strongly linked with the "carbonates" endmember in both cores. F2B is more associated with the "silicates" endmember in core BARB1-18-01 and with the "carbonates" endmember in core BARB1-18-05. F3 is more associated with the "organic matter" endmember in core BARB1-18-01 and with the "evaporites" and "silicates" endmembers in core BARB1-18-05.

4.2.4 Chronology

Short-lived radionuclides

The sedimentation rate could not be calculated from ^{210}Pbex activities for these cores. With the exception of the topmost sample in core BARB1-18-01, the F1 layer in both core tops displays little variation in ^{210}Pbex with relatively low values (between 34 and 63 mBq.g^{-1} for core BARB1-18-01 and between 53 and 72 mBq.g^{-1} for core BARB1-18-05), indicating that this layer was probably related to an event deposit (Bruel and Sabatier, 2020) (Fig. 11). Moreover, an intermediate value of ^{210}Pbex (13 mBq g^{-1} at 26 cm depth in core BARB1-18-01 and 27 mBq.g^{-1} at 12 cm depth in core BARB1-18-05), lower than those in F1 and higher than those in the underlying sediment, was measured in both profiles at the base of F1. These intermediate activities may indicate the mixing of sediment from different ages and thus erosion at the base of the F1 deposit in both cores. The topmost ^{210}Pbex activity sample (0 to 0.5 cm depth) in BARB1-18-01 displays a higher value, which could indicate present-day sedimentation after the deposition of the homogeneous thick F1 layer. There is no clear ^{137}Cs activity in cores BARB1-18-01 and BARB1-18-05 (Fig. 11). The highest ^{137}Cs activity on one sample in the homogeneous F1 event indicates that this layer is probably related to post nuclear fallout sediment remobilized in this event deposit. This allows us to date the F1 deposit after 1963 CE.

^{14}C ages

The oldest sample ^{14}C dated in sediments cored within the lagoon yields a calibrated age between 3570 and 3704 cal. BP at the base of core BARB1-18-02 (108.5 cm, Table 2). Generally, the ^{14}C dating results show many dates after 1950 and many inversions of ages. Two hypotheses can be proposed to explain these results: (1) the possibility that some of the plant macroremains used for ^{14}C dating were debris of *Thalassia testudinum* roots, whose root system can reach 80 cm below the sediment surface, resulting in ^{14}C ages much younger than the sediment at the same depth; (2) the strong hydrodynamics in the lagoon could enable the erosion and transport of old debris and mix them with younger sediment. These complex ^{14}C results prevented the construction of an age model for the cores. Nevertheless, a correlation based on sediment facies boundaries was tentatively made between the six sampled cores (Fig. 8). The bases of cores BARB1-18-01 and 02 were easily correlated with two similar thin F1 layers intercalated in F3 and a sharp transition between F3 and F2 (Fig 8). The ^{14}C ages located at the base of these two cores are also coherent (>3000 cal. BP). Thus, we decided to trust the ages located in F3 for cores BARB1-18-01 and 02. The ages near the F3-F2 transition in cores BARB1-18-05 and 06 are different: 1059 – 1255 cal. BP and 2057 – 2306 cal. BP, respectively. As core BARB1-18-05 displays a very homogenous clay without any debris in F3 and BARB1-18-06 showed more debris and plant macroremains (possibly *Thalassia testudinum* roots), we choose to trust the age in core BARB1-18-05 (1059 – 1255 cal. BP). Consequently, it appears that the F3-F2 transition was probably not synchronous in all the lagoon, with a later transition in the central part compared to the southern part of the lagoon.

https://doi.org/10.5194/nhess-2022-262
Preprint. Discussion started: 14 February 2023

Natural Hazards and Earth System Sciences
Discussions

5 Discussion

5.1 Facies interpretations and paleoenvironmental reconstitutions

Even though it was not possible to establish an accurate age model, available ages and contrasted facies successions allow us to reconstitute environmental changes that occurred in the Codrington Lagoon over the last three millennia.

~~Facies 3 (~~F3~~)~~ is located at the core bases and displays the finest grain-size (clay to silt), recording a lower-energy and more sheltered environment than the present-day lagoon. As Barbuda Island is purely carbonated, the highest values of silicates in F3 are most likely related to long-range-transported (LRT) aeolian particles brought via summer easterly Trade Winds from Africa to this island (Kumar et al., 2018), similar to what was observed over the Virgins Islands (Kumar et al., 2018) and in a lagoon of Scrub Island, located 120 km to the northwest (Biguenet et al., 2021). The highest values of silicates in F3 can be explained by smaller silicate dilution compared to other facies because of a lower sedimentation rate. F3 shows the lowest carbonate percentage (LOI950) and low Sr (CLR) content in cores BARB1-18-01 and 05 and a very low diversity and quantity of foraminifera, indicating low carbonate production. F3 in core BARB1-18-01 displays a high content of organic matter (represented by Br). In contrast, F3 in core BARB1-18-05 displays high contents of evaporitic salts (represented by Na, Cl and Mg) and silicates (represented by Fe, K, Ti, Al and Si). Brasier (1975a) showed that hypersaline lagoons generally display low foraminifera standing crops. Thus, the high Cl (CLR), low Sr (CLR) and low quantity and diversity of foraminifers in core BARB1-18-05 can be interpreted as records of a hypersaline environment, suggesting that connections between the Codrington Lagoon and the ocean were reduced during F3 deposition. Brasier (1975a) proposed that productivity in carbonated lagoons can be lowered by high organic content, generating the accumulation of toxins and leading to oxygen depletion. Thus, the large amount of Br, a proxy of organic matter, in core BARB1~~-~~18-01 could be indicative of oxygen depletion, also explaining the low diversity and quantity of foraminifera within an isolated hypersaline coastal environment (Elbaz-Poulichet et al., 2014; Sabatier et al., 2010a).

~~Facies 2 (~~F2~~)~~ is divided into two alternating subfacies: Facies 2A (F2A) and Facies 2B (F2B) (Figs. 7 and 8). The depths and thicknesses of these subfacies vary between cores, revealing lateral facies variations in the lagoon. Both F2A and F2B consist of sandy and shelly silts. F2A shows higher percentages of sand and shell fragments (EM2 and EM3) than F2B. In both subfacies, core BARB1-18-05 always shows higher percentages of coarser grain-size endmembers than core BARB1-18-01. F2A is strongly correlated with the "carbonates" endmembers in both cores, which can be partly explained by many shell fragments (100 µm to several centimeters), indicating a higher-energy environment than during F3 deposition. F2B is more influenced by the "silicates" endmember in core BARB1-18-01 and by the "carbonates" endmember in core BARB1-18-05. The relationship with the silicates endmember in core BARB1-18-01 can again be explained by lower silicate dilution compared to other facies because of the lower sedimentation rate in the area. F2B is mainly composed of a silty Mg-rich-calcite matrix with almost undamaged shells of variable size (100 µm to several centimeters) (Fig. 7) and almost no shell fragments, indicating a lower-energy environment than F2A. Moreover, FA2 and F2B both display ~~a~~ fauna dominated by abundant foraminifera individuals of *A. angulatus, P. rotunda* and many *Quinqueloculina* species, which were found living inside Codrington Lagoon by Brasier et al. ~~in (~~1975~~)~~. Furthermore, F2A and F2B display many whole and intact bivalve and gastropod shells, with more abraded shells in F2A. The identified individuals found in F2 are known to live in Codrington Lagoon (Brasier and Donahue, 1985). Thus, F2 records a more carbonated and higher-energy environment (with many broken shells in F2A), in contrast with the very shallow and enclosed lagoon recorded by F3.

https://doi.org/10.5194/nhess-2022-262
Preprint. Discussion started: 14 February 2023


Natural Hazards and Earth System Sciences
Discussions

Such an environment ~~also~~ enables the development of more oxygenated and less toxic conditions for the ~~thrive~~ thriving of rich foraminifera fauna. The presence of whole bivalves and gastropod shells and foraminifera both in F2 and in the lagoon in 1975-1985 CE indicates that the F2 depositional environment was probably similar to the modern lagoon environment (before Hurricane Irma).

The transition from the F3 to F2 environment seems to be related to relative sea level rise that led to a wider lagoon with a larger fetch allowing wind waves to develop (Fig. 1B). The two ^{14}C ages obtained in F3 are 3277-3451 cal. BP (core BARB1-18-01) and 3570-3704 cal. BP (core BARB1-18-05). They are in good agreement and correspond to a period of lower sea level, as shown by sea level records by *A. palmata* corals and microbial mats in Anguilla, Antigua, Barbuda, and Martinique (Khan et al., 2017). Khan et al. (2017) showed that the relative sea level (RSL) at 4900 cal. BP was -1.4 ± 0.5 m, indicating that during F3 deposition, the RSL was approximately 1 m below present-day sea level. Such a lower sea level could have great consequences on the shallow Codrington Lagoon, particularly in its northern part, where the average water depth is on the order of 1 m (Fig. 1C). Moreover, a lower sea level implies that the lagoon was probably not, or temporarily, connected with the ocean to the north. Indeed, this shallower sea level could explain the high content in salt and organic matter and low diversity and quantity of foraminifera indicative of an isolated coastal environment during F3 deposition.

The deepening recorded by the transition from F3 to F2 could also be explained by subsidence. Along subduction zones, the plate interface (megathrust) can rupture during large earthquakes. Between earthquakes, in the so-called interseismic period, the plate interface, which is the shallower seismogenic portion of the megathrust, is locked. In consequence, stress accumulates at the plate interface and the overriding plate deforms over several decades, centuries, or millennia. The ~~A~~area located above the locked portion of the megathrust subsides, whereas that located farther away uplifts. This deformation is suddenly released during an earthquake. When those processes are perfectly elastic, the interseismic and coseismic deformation of the upper plate are strictly of opposite sign and cancel each other (e.g., Savage, 1983). However, long term topography is building over many seismic cycles in several subduction zones (e.g., Thirumalai et al., 2015; Leclerc and Feuillet, 2019), ~~as a result of~~due to plastic deformation or slip on shallower faults. Barbuda Island is located about 170 km ~~far~~ from the trench, above the seismogenic portion of the plate interface, which undergoes vertical deformation during the seismic cycle of the megathrust (Philibosian et al., 2022). This deformation accumulates at a longer time scale over several seismic cycles to build topography (Weil-Accardo et al., 2022). Microatolls studies along the eastern coasts of the island (Hog Hole) revealed that this island subsided as a response of interseismic strain accumulation over more than five decades (1952-2005) at rate of about 5mm/yr. The sign of those vertical deformations is compatible, with that of the vertical deformation estimated with a GNSS station located few kilometers away to the west, but larger by an order of size (0.5 mm/year +/- 1 for a ~~time~~ period between 1994 and 2020, van Rijsingen et al., 2022). In this area, Weil-Accardo et al. (2022) studied a set of quaternary reef terraces and showed that the eastern part of Barbuda has undergone a long-term uplift of 0,.05 to 0.1 mm/year over the last 330 Ka. They interpreted this "permanent" deformation as a result of multiple earthquakes. In the western part of the island however, where the Codrington Lagoon is located, there is no evidence of permanent uplift and the island tends to subside over the long term. As in the eastern part, this subsidence was interpreted as a result of deformation over many seismic cycles. The Codrington Lagoon may thus have undergone alternation of coseismic subsidence events and episode of uplift during the interseismic period. However, these deformations being not perfectly elastic, residual deformation may have accumulated over many seismic cycles, causing the lagoon to subside permanently. The transition between uplift and subsidence operates over a short distance likely because Barbuda is located

https://doi.org/10.5194/nhess-2022-262
Preprint. Discussion started: 14 February 2023


Natural Hazards and Earth System Sciences
Discussions

just above the downdip limit of the seismogenic part (Weil-Accardo et al., 2022). The abrupt transition between F3 and F2 in the Codrington Lagoon could be the consequence of a sudden subsidence during a major earthquake. Interestingly, Seibert et al. (2019) found a 3500 BP old turbidite/homogenite deposit in the Barbuda basin, located offshore east of Barbuda. They concluded that this deposit ~~has~~ had been generated by a major earthquake, much larger than all historical events reported in the Lesser Antilles. Given this age is close to the transition between F3 and F2 in our cores (Fig. 8), this earthquake may have been responsible for the subsidence of Codrington Lagoon, as recorded by a deepening in the lagoon environment. Subsidence of few meters are thus expected for megathrust events comparable to Sumatra 2004 or Tohoku 2011 earthquakes (i.e., Ozawa et al., 2011).

~~Facies 1 (~~F1~~)~~ consists of fine sand (main mode at 127 µm) deposited at the top of the six cores (Figs. 7 and 8) and within five thin layers at the bottom of cores BARB1-18-01 and BARB1-18-02. Most of the F1 layers exhibit a sharp basal contact with the underlying facies, and their number decreases with increasing distance from the barrier (Fig. 8). F1 mainly consists of carbonated sand, derived from eroded fragments of marine skeletal material and of shell fragments (100 to 1000 µm). F1 displays the highest foraminifera diversity in cores BARB1-18-01 and BARB1-18-05. This fauna is dominated by autochthonous species, as observed in F2. However, the presence of rare allochthonous marine species indicates a transport from the shoreface into the lagoon during marine incursions. Given that the microtidal regime of Barbuda favors the development of an isolated lagoon (e.g., Boyd et al., 1992), as shown by historical maps and satellite images before Hurricane Irma, the presence of allochthonous species suggests an overwash of the sandy barrier. Consequently, F1 layers are interpreted as overwash deposits related to either hurricanes or tsunamis. The thin F1 layers intercalated within F3 do not present any visible tsunamigenic criteria, such as intraclasts of underlying sediment or mud caps. Given that hurricanes occur much more frequently than tsunamis in Barbuda, we assume that F1 layers intercalated with F3 could record hurricane events. However, it is also possible that one of the F1 layers intercalated in F3 corresponds to the potential 3500 cal. BP tsunami event recorded by the turbidite/homogenite (Seibert et al., 2019). The F1 layer at the top of cores BARB1-18-~~-~~01 and BARB1-18-05 display rather homogeneous ^{210}Pbex values, indicating deposition of the F1 layer triggered by a single rapid event reworking previously deposited material (Fig. 10, Bruel and Sabatier, 2020). Moreover, both ^{210}Pbex profiles exhibit an intermediate value at the base of F1, which may indicate the mixing of sediment from different ages and thus erosion at the base of the F1 deposit. From these observations, we assume that the thick F1 sand layer deposited at the top of the six cores corresponds to a unique high-energy and instantaneous marine flooding event that occurred recently, before core sampling in March 2018 and after the maximum bomb test radionuclide fallout (1963). As no tsunami occurred in Barbuda during this period, the best candidate for this deposit is a hurricane (Fig. 2).

5.2 Hurricane activity since 1750 and morphological evolution of the Codrington Lagoon

From 1750 CE to 1973 CE, nine hurricanes, with intensities from one to four, passed within 30 km from Codrington Lagoon (Table 1; NOAA, 2021, historical hurricane tracks). Given no nautical maps (Fig. 3) or historical record indicated the presence of any inlet in the barrier during this period, we assume that none of these hurricanes generated a breach ~~enough~~ wide and deep enough to evolve toward an inlet through the sandy western barrier. Moreover, satellite images from 1982 to 2017 show a continuous sandy barrier despite the occurrence of four hurricanes of category one to four that passed within 30 km from Codrington Lagoon (Table 1; NOAA, 2021, Historical Hurricane Tracks; Fig. 4). A washover fan is visible on the December 1999 satellite image to the south of the barrier but did not exist on the previous image of May 1992. Hurricanes Luis (H4) and Bertha (H1), which occurred in 1995 and 1996, respectively, could be good

https://doi.org/10.5194/nhess-2022-262
Preprint. Discussion started: 14 February 2023


Natural Hazards and Earth System Sciences Discussions

candidates to explain this washover. Potter et al., (2017) mentioned a narrow breach that emplaced across the barrier after Hurricane Luis. Unfortunately, images without clouds are not available between 1995 and 1999 to confirm this observation. However, given that Luis was much stronger than Bertha and Luis made landfall on Barbuda (Table 1; Fig. 2), it is likely that Luis was able to produce the washover observed in 1999. Following Category 5 Hurricane Irma (September 2017), two wide inlets, 0.5 and 1.2 km-wide, developed and were observed in November 2017 (Fig. 4). The southern inlet closed between March and July 2018 (Fig. 4). In contrast, the northern inlet became larger and was still open in September 2021. Seismic profiling within this inlet in June 2021 shows that a large and thick ebb tidal and a 1-m-thick sand sheet developed within the main channel. The permanent opening of a wide inlet 5 years after Hurricane Irma across the sandy barrier supports the idea that this extreme event was exceptional. The permanence of such a wide inlet in a wave-dominated and microtidal environment might seem surprising. Indeed, the stability of tidal inlets can be related to the ratio between the tidal prism (Ω) and the annual net littoral drift (M) (Bruun et al., 1978): the stability of tidal inlets decreases with decreasing Ω /M. Thus, in a microtidal setting (reduced tidal prism), the tidal inlet tends to be filled by sediment transported by wave-related processes, such as littoral drift and/or cross shore sand transport. Nevertheless, it can be assumed that along the west coast of Barbuda, waves are very attenuated, leading to small littoral drift, explaining why the inlet remains open. Another hypothesis is related to wind stress on the large surface area of the Codrington Lagoon, related to NE trade winds, that ~~is able to~~can induce strong seaward currents across the inlet.

5.3 Hurricane Irma: an exceptional event

From available data, no wide barrier breach or tidal inlet similar to those developed after Hurricane Irma was documented in Codrington Lagoon. Assuming the Codrington Lagoon barrier remained continuous for more than 250 years, the opening of a wide inlet after Hurricane Irma is an argument for the exceptional character of this event. Thus, inlet opening after major hurricanes have already been reported in other areas (e.g., Sallenger et al., 2006; Chaumillon et al., 2014; Safak et al., 2016). Hurricane Irma also generated beaches erosion in many islands such as in Saint Martin and Saint-Barthelemy islands (Rey et al., 2019), in Anegada Island (Spiske et al., 2021), or Marco Island in Florida (Harvey, 2021).

Moreover, sediment cores show that the upper Codrington lagoon fill consists of a recent and sharp-based fine sand sheet (F1) deposited upon the silty lagoon facies (F2). We interpret this sand sheet as recording the devastating passage of Hurricane Irma. This event induced a significant storm surge with a peak water level ~~at~~ of 2.4 m, with ~~means higher high water (~~MHHW~~)~~ recorded at a tide gauge on the island. Such exceptionally high sea levels were due to the combined effects of storm surge (resulting from low pressure effect and wind stress), wave setup, swash and infragravity waves (e.g., Chaumillon et al., 2017) and allowed overwashing of the 1- to 3-m-high sandy barrier. The required sand supply for such a thick and extensive unit would originate from both the breached and eroded sandy barrier and the sandy shoreface. Near the inlet, the sand supply also probably originated from the flood tidal delta. The sandy shoreface origin of this sand supply is supported by the occurrence of allochthonous foraminifera originating from outside the lagoon. Given that this thick sand sheet is unique at the scale of the sediment cores recording a lagoon story longer than 3700 years, it seems that the event responsible for this sand sheet had no equivalent over the last millennia.

Nevertheless, one major limitation of our sedimentological study is related to the absence of an accurate age model and to ^{14}C age inversions. Thus, we cannot rule out that the sedimentation within the lagoon was not continuous and that some hurricanes were not recorded and/or were eroded. However, the thickness and the lateral extension of the upper F1 sand sheet argue for the unlikeliness of analogous older hurricane records. Another main limitation of our study is related to

https://doi.org/10.5194/nhess-2022-262
Preprint. Discussion started: 14 February 2023

Natural Hazards and Earth System Sciences
Discussions

changes in relative sea level and/or vertical motions during the last 3700 years that can drastically change the sensitivity of the lagoon to overwash~~es~~ and marine floods. Moreover, the lagoon and barrier morphology has likely changed during the last 3700 years, and we do not have any information about those changes prior to the oldest marine map (1750-1785 CE, Fig. 3). These limitations do not allow us to firmly conclude whether the Irma Hurricane was unique at the scale of the last 3700 years.

Even if other~~s~~ events of this intensity occurred in Barbuda Island during the last 3700 years, the consequences of Hurricane Irma remain exceptional in the current climate change context. Thus, the opening of the current lagoon barrier has left the island more exposed to future major hurricanes. This phenomenon has already been observed in a Southwest Florida back-barrier lagoon, where the almost complete disappearance of a separate barrier that was once seaward of the current barrier island foreshore occurred during the period that saw the passing of Hurricane Donna (1960 CE). This event was the most significant hurricane to have impact in the southwest Florida region during modern historical time and has left the island more exposed to major storm events such as Hurricane Irma (Martin and Muller, 2021).

As extreme seasons with category 4-5 hurricanes might be more regular in the future due to current and projected atmospheric and oceanic warming (Pfleiderer et al., 2022), hurricane overwash events and coastal flooding will likely become more prevalent. This increase of major hurricane~~s~~ associated ~~to the~~with sea level rise exposes a growing number of low-~~–~~lying coasts and islands to marine submersion, especially barrier islands, which are extremely vulnerable landscapes. Thus, it is crucial to understand the coastline geomorphological and sedimentological changes in response to hurricane processes to better inform and prepare coastal communities. More specifically, understanding potential areas of overwash and erosion vulnerability will be crucial for future decisions around coastal resilience and infrastructure planning (Martin and Muller, 2021).

6 Conclusion

From available satellite images (1982–2021) and old nautical maps (1750-1785 to 1973 CE) prior to Hurricane Irma, the Codrington Lagoon sandy barrier probably remained continuous for at least the last 250 years. No large barrier breaching occurred during the 1990 – 2000 CE period, despite the occurrence of four hurricanes, of category one to four, that passed within 30 km from Codrington Lagoon. However, following Category 5 Hurricane Irma, two ~~wide~~ inlets of 0.5 and 1.2 km wide developed. The southern inlet has since been closed, but the northern inlet enlarged and was still open in September 2021. This inlet allowed the development of a large and thick ebb delta offshore, as shown by seismic profiling. The permanent opening of a wide inlet 5 years after Hurricane Irma across a sandy barrier that has remained continuous for more than 250 years supports the idea that this hurricane was exceptional. Sedimentological, geochemical, microfaunal and chronological analyses conducted on six sediment cores sampled in Codrington Lagoon seven months after the event showed that Irma led to the deposition of a thick sediment layer in all coring locations, which had no equivalent over the last 3 millennia. Despite limitations related to the absence of an accurate age model and information about the morphological evolution of the lagoon during the last millenaries, the sediment record, together with satellite images and old nautical maps, seem to show that Hurricane Irma was exceptional and perhaps unique for the last 3700 years. Our results seem to ~~be in agreement~~agree with the occurrence of hurricanes with unprecedented intensities related to present-day global warming. However, given uncertainties related to geomorphological data and sedimentological records, complementary studies need to be pursued in other lagoons of the Caribbean.

https://doi.org/10.5194/nhess-2022-262
Preprint. Discussion started: 14 February 2023

Natural Hazards and Earth System Sciences
Discussions

Data availability

All raw data can be provided by the corresponding authors upon request.

Supplement

The supplement related to this article is available online at:

Author contribution

MB, EC, PS, FA, TC and NF participated ~~to~~ in the fieldwork; MB, AB and EG performed the measurements and analyzed the data; MB wrote the manuscript draft; EC, PS, FA, TC and NF reviewed and edited the manuscript.

Competing interests

The authors declare that they have no conflict of interest.

Acknowledgments

This work is part of the CARQUAKES project (ANR-17-CE03-0006). The authors would like to thank the Ministry of Foreign Affairs, Immigration and Trade of Antigua and Barbuda for permitting core sampling and geophysical surveying in Codrington Lagoon. The authors thank skipper Nicolas Jammes, who was involved in the March 2018 field survey. We thank the GENAVIR captain, officers and crew of R/V ANTEA (Flotte Océanographique Française) and scientific cruise party, who were involved in the June 2021 field survey. We also thank Louise Cordrie for her valuable support during the 2021 field mission. We thank the Laboratoire Souterrain de Modane (LSM) facilities for the gamma spectrometry measurements. We thank the LMC14 staff (Laboratoire de Mesure du Carbone-14), ARTEMIS national facility, (LSCE (CNRS-CEA-UVSQ)-IRD-IRSN-MC) for the results obtained with the accelerator mass spectrometry method. The authors would like to thank the EDYTEM laboratory for the X-ray fluorescence analyses and Fayçal Soufi for his involvement in the realization of the thin sections. The authors thank Pierre Vacher and the Symme Laboratory (Annecy, France) for the authorization to scan core BARB1-18-01 using the X-ray tomography system Easytom XL 150 from the RX SOLUTION Society.

Financial support

This work was supported by the CARQUAKES project (ANR-17-CE03-0006) from the French national research agency (Agence Nationale de la Recherche).

https://doi.org/10.5194/nhess-2022-262
Preprint. Discussion started: 14 February 2023

Natural Hazards and Earth System Sciences Discussions

References

Abu-Zied, R.H., Bantan, R.A., 2013. Hypersaline benthic foraminifera from the Shuaiba Lagoon, eastern Red Sea, Saudi Arabia: Their environmental controls and usefulness in sea-level reconstruction. Marine Micropaleontology 103, 51–67. https://doi.org/10.1016/j.marmicro.2013.07.005

Atwater, B.F., ten Brink, U.S., Cescon, A.L., Feuillet, N., Fuentes, Z., Halley, R.B., Nuñez, C., Reinhardt, E.G., Roger, J.H., Sawai, Y., Spiske, M., Tuttle, M.P., Wei, Y., Weil-Accardo, J., 2017. Extreme waves in the British Virgin Islands during the last centuries before 1500 CE. Geosphere 13, 301–368. https://doi.org/10.1130/GES01356.1

Bacopoulos, P., 2019. Extreme low and high waters due to a large and powerful tropical cyclone: Hurricane Irma (2017). Nat Hazards 98, 939–968. https://doi.org/10.1007/s11069-018-3327-7

Bain, A., Faucher, A.-M., Kennedy, L.M., LeBlanc, A.R., Burn, M.J., Boger, R., Perdikaris, S., 2018. Landscape ~~Transformation~~ transformation ~~During~~ during ~~Ceramic~~ ceramic ~~Age~~ age and ~~Colonial~~ colonial ~~Occupations~~ occupations of Barbuda, West Indies. Environmental Archaeology 23, 36–46. https://doi.org/10.1080/14614103.2017.1345115

Bajard, M., Sabatier, P., David, F., Develle, A.-L., Reyss, J.-L., Fanget, B., Malet, E., Arnaud, D., Augustin, L., Crouzet, C., Poulenard, J., Arnaud, F., 2016. Erosion record in Lake La Thuile sediments (Prealps, France): Evidence of montane landscape dynamics throughout the Holocene. The Holocene 26, 350–364. https://doi.org/10.1177/0959683615609750

Berg, R., 2018. National Hurricane Center tropical cyclone report: Hurricane Jose. NOAA/NWS Rep. AL112017.

Bernard, P., Lambert, J., 1988. Subduction and seismic hazard in the northern Lesser Antilles: Revision of the historical seismicity. Bulletin of the Seismological Society of America 78, 1965–1983.

Bhatia, K.T., Vecchi, G.A., Knutson, T.R., Murakami, H., Kossin, J., Dixon, K.W., Whitlock, C.E., 2019. Recent increases in tropical cyclone intensification rates. Nat Commun 10, 635. https://doi.org/10.1038/s41467-019-08471-z

Biguenet, M., Sabatier, P., Chaumillon, E., Chagué, C., Arnaud, F., Jorissen, F., Coulombier, T., Geba, E., Cordrie, L., Vacher, P., Develle, A.L., Chalmin, E., Soufi, F., Feuillet, N., 2021. A 1600 year-long sedimentary record of tsunamis and hurricanes in the Lesser Antilles (Scrub Island, Anguilla). Sedimentary Geology 412, 105806. https://doi.org/10.1016/j.sedgeo.2020.105806

Boger, R., Low, R., Nelson, P., 2020. Identifying hurricane impacts on Barbuda using citizen science ground observations, drone photography and satellite imagery. Int. Arch. Photogramm. Remote Sens. Spatial Inf. Sci. XLII-3/W11, 23–28. https://doi.org/10.5194/isprs-archives-XLII-3-W11-23-2020

Boyd, R., Dalrymple, R., Zaitlin, B.A., 1992. Classification of clastic coastal depositional environments. Sedimentary Geology, Research Conference on Quaternary Coastal Evolution 80, 139–150. https://doi.org/10.1016/0037-0738(92)90037-R

Brasier, M.D., 1975a. Ecology of ~~Recent~~ recent sediment-dwelling and phytal foraminifera from the lagoons of Barbuda, West Indies. Journal of Foraminiferal Research 5, 42–61. https://doi.org/10.2113/gsjfr.5.1.42

Brasier, M.D., 1975b. The ecology and distribution of ~~Recent~~ recent foraminifera from the reefs and shoals around Barbuda, West Indies. Journal of Foraminiferal Research 5, 193–210. https://doi.org/10.2113/gsjfr.5.3.193

Brasier, Donahue, 1985. Barbuda-an emerging reef and lagoon complex on the edge of the Lesser Antilles ~~island~~ Island arc 17.

Breilh, J.F., Chaumillon, E., Bertin, X., Gravelle, M., 2013. Assessment of static flood modeling techniques: application to contrasting marshes flooded during Xynthia (western France). Natural Hazards and Earth System Sciences 13, 1595–1612. https://doi.org/10.5194/nhess-13-1595-2013

https://doi.org/10.5194/nhess-2022-262
Preprint. Discussion started: 14 February 2023

Bruel, R., Sabatier, P., 2020. serac: A R package for ShortlivEd RAdionuclide chronology of recent sediment cores. Journal of Environmental Radioactivity 225, 106449. https://doi.org/10.1016/j.jenvrad.2020.106449

Bruun, P., Mehta, A.J., Johnsson, I.G., 1978. Stability of Tidal Inlets. Theory and Engineering. Elsevier Scientific 506.

Burn, M.J., Holmes, J., Kennedy, L.M., Bain, A., Marshall, J.D., Perdikaris, S., 2016. A sediment-based reconstruction of Caribbean effective precipitation during the 'Little Ice Age' from Freshwater Pond, Barbuda. The Holocene 26, 1237–1247. https://doi.org/10.1177/0959683616638418

Cangialosi, J.P., Latto, A.S., Berg, R., 2018. National Hurricane Center tropical cyclone report: Hurricane Irma. NOAA/NWS Rep. AL112017, 111 pp.

Chagué-Goff, C., Fyfe, W.S., 1996. Geochemical and petrographical characteristics of a domed bog, Nova Scotia: a modern analogue for temperate coal deposits. Organic Geochemistry, The Society for Organic Petrology 24, 141–158. https://doi.org/10.1016/0146-6380(96)00014-9

Chagué-Goff, C., Szczuciński, W., Shinozaki, T., 2017. Applications of geochemistry in tsunami research: A review. Earth-Science Reviews 165, 203–244. https://doi.org/10.1016/j.earscirev.2016.12.003

Chaumillon, E., Bertin, X., Falchetto, H., Allard, J., Weber, N., Walker, P., Pouvreau, N., Woppelmann, G., 2008. Multi time-scale evolution of a wide estuary linear sandbank, the Longe de Boyard, on the French Atlantic coast. Marine Geology 251, 209–223. https://doi.org/10.1016/j.margeo.2008.02.014

Chaumillon, E., Florian, O., Xavier, B., Nathalie, L., Florian, G., 2014. Control of wave climate and meander dynamics on spit breaching and inlet migration. Journal of Coastal Research 70, 109–114. https://doi.org/10.2112/SI70-019.1

Chaumillon, E., Bertin, X., Fortunato, A.B., Bajo, M., Schneider, J.-L., Dezileau, L., Walsh, J.P., Michelot, A., Chauveau, E., Créach, A., Hénaff, A., Sauzeau, T., Waeles, B., Gervais, B., Jan, G., Baumann, J., Breilh, J.-F., Pedreros, R., 2017. Storm-induced marine flooding: Lessons from a multidisciplinary approach. Earth-Science Reviews 165, 151–184. https://doi.org/10.1016/j.earscirev.2016.12.005

Chester, D.K., 2001. The 1755 Lisbon earthquake. Progress in Physical Geography: Earth and Environment 25, 363–383. https://doi.org/10.1177/030913330102500304

Cordrie, L., Escartin, J., Gailler, A., Feuillet, N., Heinrich, P., 2019. Simulation of the 2004 tsunami of Les Saintes in Guadeloupe (Lesser Antilles), in: OCEANS 2019 - Marseille. Presented at the OCEANS 2019 - Marseille, IEEE, Marseille, France, pp. 1–9. https://doi.org/10.1109/OCEANSE.2019.8867447

Cordrie, L., Feuillet, N., Gailler, A., Biguenet, M., Chaumillon, E., Sabatier, P., 2022. A Megathrust earthquake as source of a Pre-Colombian tsunami in Lesser Antilles: Insight from sediment deposits and tsunami modeling. Earth-Science Reviews 228, 104018. https://doi.org/10.1016/j.earscirev.2022.104018

Cornée, J.-J., Münch, P., Philippon, M., BouDagher-Fadel, M., Quillévéré, F., Melinte-Dobrinescu, M., Lebrun, J.-F., Gay, A., Meyer, S., Montheil, L., Lallemand, S., Marcaillou, B., Laurencin, M., Legendre, L., Garrocq, C., Boucard, M., Beslier, M.-O., Laigle, M., Schenini, L., Fabre, P.-H., Antoine, P.-O., Marivaux, L., 2021. Lost islands in the northern Lesser Antilles: possible milestones in the Cenozoic dispersal of terrestrial organisms between South-America and the Greater Antilles. Earth-Science Reviews 217, 103617. https://doi.org/10.1016/j.earscirev.2021.103617

DeMets, C., Jansma, P.E., Mattioli, G.S., Dixon, T.H., Farina, F., Bilham, R., Calais, E., Mann, P., 2000. GPS geodetic constraints on Caribbean-North America Plate Motion. Geophysical Research Letters 27, 437–440. https://doi.org/10.1029/1999GL005436

https://doi.org/10.5194/nhess-2022-262
Preprint. Discussion started: 14 February 2023

Denommee, K.C., Bentley, S.J., Droxler, A.W., 2015. Climatic controls on hurricane patterns: a 1200-y near-annual record from Lighthouse Reef, Belize. Scientific Reports 4. https://doi.org/10.1038/srep03876

Donnelly, J.P., Woodruff, J.D., 2007. Intense hurricane activity over the past 5,000 years controlled by El Niño and the West African monsoon. Nature 447, 465–468. https://doi.org/10.1038/nature05834

Donnelly, J.P., Hawkes, A.D., Lane, P., MacDonald, D., Shuman, B.N., Toomey, M.R., van Hengstum, P.J., Woodruff, J.D., 2015. Climate forcing of unprecedented intense-hurricane activity in the last 2000 years. Donnelly et al. Earth's Future 3, 49–65. https://doi.org/10.1002/2014EF000274

Dorel, J., 1981. Seismicity and seismic gap in the Lesser Antilles arc and earthquake hazard in Guadeloupe. Geophysical Journal of the Royal Astronomical Society 67, 679–695. https://doi.org/10.1111/j.1365-246X.1981.tb06947.x

Dunn, G.E., 1961. The Hurricane season of 1960. Monthly Weather Review.

Elbaz-Poulichet, F., Sabatier, P., Dezileau, L., Freydier, R., 2014. Sedimentary record of V, U, Mo and Mn in the Pierre-Blanche lagoon (Southern France) – Evidence for a major anoxia event during the Roman period. The Holocene 24, 1384–1392. https://doi.org/10.1177/0959683614540957

Engel, M., Oetjen, J., May, S.M., Brückner, H., 2016. Tsunami deposits of the Caribbean – Towards an improved coastal hazard assessment. Earth-Science Reviews 163, 260–296. https://doi.org/10.1016/j.earscirev.2016.10.010

Feuillet, N., Beauducel, F., Tapponnier, P., 2011. Tectonic context of moderate to large historical earthquakes in the Lesser Antilles and mechanical coupling with volcanoes. Journal of Geophysical Research 116. https://doi.org/10.1029/2011JB008443

Fuentes, Z., Tuttle, M.P., Schmidt, W.E., 2017. Sand Scripts of Past Tsunamis in Coastal Ponds of St. Thomas, U.S. Virgin Islands. Seismological Research Letters 88, 1516–1526. https://doi.org/10.1785/0220170038

Fullarton, A. & Co., 1872. The West Indies. By G.H. Swanston, Edinr. (with) The Most Important Of The Lesser British Islands On An Enlarged Scale. LXI. Engraved. by G.H. Swanston Edinburgh. A. Fullarton & Co. Edinburgh, London & Dublin. [Accessed in October 2021 from David Rumsey Map Collection (http://www.davidrumsey.com/maps3022.html)]

Gerritsen, H., 2005. What happened in 1953? The Big Flood in the Netherlands in retrospect. Philosophical Transactions of the Royal Society A: Mathematical, Physical and Engineering Sciences 363, 1271–1291. https://doi.org/10.1098/rsta.2005.1568

Glumac, B., Curran, H.A., 2016. Documentation of Extensive Root Systems of Thalassia Seagrass Along the Banks of Pigeon Creek, San Salvador Island, Bahamas. Presented at the proceedings of the 16th symposium on the geology of the Bahamas and other carbonate regions, Gerace Research Centre San Salvador, Bahamas, p. 11.

Goldberg, E.G., 1963. Geochronology with 210Pb. Radioactive Dating, International Atomic Energy Agency, Vienna, 121–131.

Griffis, F.H. (Bud), 2007. Engineering failures exposed by Hurricane Katrina. Technology in Society, Perspectives on Hurricane Katrina 29, 189–195. https://doi.org/10.1016/j.techsoc.2007.01.015

Harbitz, C.B., Glimsdal, S., Bazin, S., Zamora, N., Løvholt, F., Bungum, H., Smebye, H., Gauer, P., Kjekstad, O., 2012. Tsunami hazard in the Caribbean: Regional exposure derived from credible worst case scenarios. Continental Shelf Research 38, 1–23. https://doi.org/10.1016/j.csr.2012.02.006

Harvey, N., 2021. Geomorphological impact of Hurricane Irma on Marco Island, Southwest Florida. Natural Hazards 17.

Heiri, O., Lotter, A.F., Lemcke, G., 2001. Loss on ignition as a method for estimating organic and carbonate content in sediments: reproducibility and comparability of results. Journal of Paleolimnology 25, 101–110.

https://doi.org/10.5194/nhess-2022-262
Preprint. Discussion started: 14 February 2023

Natural Hazards and Earth System Sciences
Discussions

Hoggarth, D., 2001. Management Plan for the Marine Parks of Anguilla. Prepared for: Organisation of Eastern Caribbean States Natural Resources Management Unit St Lucia. Department for International Development 65.

Holland, G., Bruyère, C.L., 2014. Recent intense hurricane response to global climate change. Clim Dyn 42, 617–627. https://doi.org/10.1007/s00382-013-1713-0

Hough, S.E., 2013. Missing great earthquakes. Journal of Geophysical Research: Solid Earth 118, 1098–1108. https://doi.org/10.1002/jgrb.50083

James, P., 2003. Analysis of beach changes in Antigua and Barbuda 1996- 2001 (Assessment Report No. Volume 1). Fisheries Division, Ministry of Agriculture, Lands, Fisheries, Antigua and Barbuda, Antigua and Barbuda.

Javaux, E.J., Scott, D.B., 2003. Illustration of ~~Modern~~ modern ~~Benthic~~ benthic ~~Foraminifera~~ foraminifera from Bermuda and ~~Remarks~~ remarks on ~~Distribution~~ distribution in ~~Other~~ other ~~Subtropical~~subtropical/~~Tropical~~ tropical ~~Areas~~areas. Palaeontologia Electronica 6, 29.

Karim, M.F., Mimura, N., 2008. Impacts of climate change and sea-level rise on cyclonic storm surge floods in Bangladesh. Global Environmental Change, Globalisation and Environmental Governance: Is Another World Possible? 18, 490–500. https://doi.org/10.1016/j.gloenvcha.2008.05.002

Khan, N.S., Ashe, E., Horton, B.P., Dutton, A., Kopp, R.E., Brocard, G., Engelhart, S.E., Hill, D.F., Peltier, W.R., Vane, C.H., Scatena, F.N., 2017. Drivers of Holocene sea-level change in the Caribbean. Quaternary Science Reviews 155, 13–36. https://doi.org/10.1016/j.quascirev.2016.08.032

Knowles, J.T., 2008. A 5000-year history of Caribbean environmental change and hurricane activity reconstructed from coastal lake sediments of the West Indies.

Knutson, T., Camargo, S.J., Chan, J.C.L., Emanuel, K., Ho, C.-H., Kossin, J., Mohapatra, M., Satoh, M., Sugi, M., Walsh, K., Wu, L., 2019. Tropical Cyclones and Climate Change Assessment: Part I: Detection and Attribution. Bulletin of the American Meteorological Society 100, 1987–2007. https://doi.org/10.1175/BAMS-D-18-0189.1

Kossin, J.P., Olander, T.L., Knapp, K.R., 2013. Trend Analysis with a New Global Record of Tropical Cyclone Intensity. Journal of Climate 26, 9960–9976. https://doi.org/10.1175/JCLI-D-13-00262.1

Kossin, J.P., Knapp, K.R., Olander, T.L., Velden, C.S., 2020. Global increase in major tropical cyclone exceedance probability over the past four decades. Proceedings of the National Academy of Sciences 117, 11975–11980. https://doi.org/10.1073/pnas.1920849117

Kumar, A., Abouchami, W., Galer, S.J.G., Singh, S.P., Fomba, K.W., Prospero, J.M., Andreae, M.O., 2018. Seasonal radiogenic isotopic variability of the African dust outflow to the tropical Atlantic Ocean and across to the Caribbean. Earth and Planetary Science Letters 487, 94–105. https://doi.org/10.1016/j.epsl.2018.01.025

Lander, J.F., Whiteside, L.S., Lockridge, P.A., 2002. A brief history of tsunamis in the Caribbean ~~sea~~Sea. Science of Tsunami Hazards 20, 57.

Leclerc, F.E., Feuillet, N., 2019. Quaternary coral reef complexes as markers of long-term subduction-induced subsidence. Geosphere. https://doi.org/10.1130/GES02069.1

Liu, Y., Liu, X., Sun, Y., 2021. QGrain: An open-source and easy-to-use software for the comprehensive analysis of grain size distributions. Sedimentary Geology 423, 105980. https://doi.org/10.1016/j.sedgeo.2021.105980

Malaizé, B., Bertran, P., Carbonel, P., Bonnissent, D., Charlier, K., Galop, D., Imbert, D., Serrand, N., Stouvenot, Ch., Pujol, C., 2011. Hurricanes and climate in the Caribbean during the past 3700 years BP. The Holocene 21, 911–924. https://doi.org/10.1177/0959683611400198

Martin, T., Muller, J., 2021. The geologic record of Hurricane Irma in a Southwest Florida back-barrier lagoon. Marine Geology 441, 106635. https://doi.org/10.1016/j.margeo.2021.106635

https://doi.org/10.5194/nhess-2022-262
Preprint. Discussion started: 14 February 2023

Mccann, W.R., Dewey, J.W., Murphy, A.J., Harding, S.T., 1982. A large normal-fault earthquake in the overriding wedge of the Lesser Antilles subduction zone: the earthquake of 8 October 1974. Bulletin of the Seismological Society of America 72, 2267–2283.

McCloskey, T.A., Keller, G., 2009. 5000 year sedimentary record of hurricane strikes on the central coast of Belize. Quaternary International 195, 53–68. https://doi.org/10.1016/j.quaint.2008.03.003

NGDC/WDS (National Geophysical Data Center/World Data Service), 2020. Global Historical Tsunami Database. National Geophysical Data Center, NOAA https://doi.org/ 10.7289/V5PN93H7. (Accessed 10 December 2020).

NOAA (National Oceanic and Atmospheric Administration), 2021. Historical Hurricane Tracks. https://coast.noaa.gov/hurricanes/#map=4/32/-80. (Accessed 15 October 2021).

Oliver, V.L., 1894. The history of the island of Antigua, one of the Leeward Caribbees in the West Indies, from the first settlement in 1635 to the present time. London, Mitchell and Hughes.

Ozawa, S., Nishimura, T., Suito, H., Kobayashi, T., Tobita, M., Imakiire, T., 2011. Coseismic and postseismic slip of the 2011 magnitude-9 Tohoku-Oki earthquake. Nature 475, 373–376. https://doi.org/10.1038/nature10227

Pelinovsky, E., Zahibo, N., Dunkley, P., Edmonds, M., Herd, R., Talipova, T., Kozelkov, A., Nikolkina, I., 2004. Tsunami ~~Generated~~ generated ~~By~~ by the ~~Volcano~~ volcano ~~Eruption~~ eruption ~~On~~ on July 12-13, 2003 ~~At~~ at Montserrat, Lesser Antilles. Science of Tsunami Hazards 22, 15.

Pfleiderer, P., Nath, S., Schleussner, C.-F., 2022. Extreme Atlantic hurricane seasons made twice as likely by ocean warming. Weather and Climate Dynamics 3, 12.

Philibosian, B., Feuillet, N., Weil-Accardo, J., Jacques, E., Guihou, A., Mériaux, A.-S., Anglade, A., Saurel, J.-M., Deroussi, S., 2022. 20th-century strain accumulation on the Lesser Antilles megathrust based on coral microatolls. Earth and Planetary Science Letters 579, 117343. https://doi.org/10.1016/j.epsl.2021.117343

Potter, A.E., Chenoweth, S., Day, M., 2017. Antigua and Barbuda, in: Allen, C.D. (Ed.), Landscapes and Landforms of the Lesser Antilles, World Geomorphological Landscapes. Springer International Publishing, Cham, pp. 99–116. https://doi.org/10.1007/978-3-319-55787-8_8

R Core Team, 2020. R: A language and environment for statistical computing. R Foundation for Statistical Computing, Vienna, Austria. [WWW Document]. URL http://www.r-project.org/index.html

Reid, H.F., Taber, S., 1920. ~~THE~~ The ~~VIRGIN~~ Virgin ~~ISLANDS~~ Islands ~~EARTHQUAKES~~ Earthquakes ~~OF~~ of 1867-1868. Bull. Seismol. Soc. Am. 10, 9– 30.

Reimer, P.J., Bard, E., Bayliss, A., Beck, J.W., Blackwell, P.G., Ramsey, C.B., Buck, C.E., Cheng, H., Edwards, R.L., Friedrich, M., Grootes, P.M., Guilderson, T.P., Haflidason, H., Hajdas, I., Hatté, C., Heaton, T.J., Hoffmann, D.L., Hogg, A.G., Hughen, K.A., Kaiser, K.F., Kromer, B., Manning, S.W., Niu, M., Reimer, R.W., Richards, D.A., Scott, E.M., Southon, J.R., Staff, R.A., Turney, C.S.M., van der Plicht, J., 2013. IntCal13 and Marine13 Radiocarbon Age Calibration Curves 0–50,000 Years cal BP. Radiocarbon 55, 1869–1887. https://doi.org/10.2458/azu_js_rc.55.16947

Rey, T., Leone, F., Candela, T., Belmadani, A., Palany, P., Krien, Y., Cécé, R., Gherardi, M., Péroche, M., Zahibo, N., 2019. Coastal Processes and Influence on Damage to Urban Structures during Hurricane Irma (St-Martin & St-Barthélemy, French West Indies). JMSE 7, 215. https://doi.org/10.3390/jmse7070215

Reyss, J.-L., Schmidt, S., Legeleux, F., Bonté, P., 1995. Large, low background well-type detectors for measurements of environmental radioactivity. Nuclear Instruments and Methods in Physics Research Section A: Accelerators,

https://doi.org/10.5194/nhess-2022-262
Preprint. Discussion started: 14 February 2023

Spectrometers, Detectors and Associated Equipment 357, 391–397. https://doi.org/10.1016/0168-9002(95)00021-6

Richter, T.O., van der Gaast, S., Koster, B., Vaars, A., Gieles, R., de Stigter, H.C., De Haas, H., van Weering, T.C.E., 2006. The Avaatech XRF Core Scanner: technical description and applications to NE Atlantic sediments. Geological Society, London, Special Publications 267, 39–50. https://doi.org/10.1144/GSL.SP.2006.267.01.03

Roger, J., Baptista, M.A., Sahal, A., Accary, F., Allgeyer, S., Hébert, H., 2011. The Transoceanic 1755 Lisbon Tsunami in Martinique. Pure and Applied Geophysics 168, 1015–1031. https://doi.org/10.1007/s00024-010-0216-8

Sabatier, P., Dezileau, L., Barbier, M., Raynal, O., Lofi, J., Briqueu, L., Condomines, M., Bouchette, F., Certain, R., Van Grafenstein, U., Jorda, C., Blanchemanche, P., 2010. Late-Holocene evolution of a coastal lagoon in the Gulf of Lions (South of France). Bulletin de la Societe Geologique de France 181, 27–36. https://doi.org/10.2113/gssgfbull.181.1.27

Sabatier, Pierre, Dezileau, L., Briqueu, L., Colin, C., Siani, G., 2010. Clay minerals and geochemistry record from northwest Mediterranean coastal lagoon sequence: Implications for paleostorm reconstruction. Sedimentary Geology 228, 205–217. https://doi.org/10.1016/j.sedgeo.2010.04.012

Safak, I., Warner, J.C., List, J.H., 2016. Barrier island breach evolution: Alongshore transport and bay-ocean pressure gradient interactions. Journal of Geophysical Research: Oceans 121, 8720–8730. https://doi.org/10.1002/2016JC012029

Sainte-Claire Deville, C., 1843. Observations sur le tremblement de terre éprouvé à la Guadeloupe le 8 Février 1843. Imprimerie du Gouverneur, Basse-Terre.

Sallenger, A.H., Stockdon, H.F., Fauver, L., Hansen, M., Thompson, D., Wright, C.W., Lillycrop, J., 2006. Hurricanes 2004: An overview of their characteristics and coastal change. Estuaries and Coasts: J ERF 29, 880–888. https://doi.org/10.1007/BF02798647

Savage, J.C., 1983. A dislocation model of strain accumulation and release at a subduction zone. Journal of Geophysical Research: Solid Earth 88, 4984–4996. https://doi.org/10.1029/JB088iB06p04984

Schindelin, J., Arganda-Carreras, I., Frise, E., Kaynig, V., Longair, M., Pietzsch, T., Preibisch, S., Rueden, C., Saalfeld, S., Schmid, B., Tinevez, J.-Y., White, D.J., Hartenstein, V., Eliceiri, K., Tomancak, P., Cardona, A., 2012. Fiji: an open-source platform for biological-image analysis. Nature Methods 9, 676–682. https://doi.org/10.1038/nmeth.2019

Seibert C., Feuillet N., Beck C., Ducassou E., Morena P., Johannes L., Ratzov G., Goldfinger C., Cattaneo A., Moreno E., 2019. Long Term Recurrence of Deeply Ponded Turbidites and Thick Homogenites in the Lesser Antilles Forearc: Imprint of Great Earthquakes [abstract]. In: American Geophysical Union, Fall Meeting; 2019 December 9 – 13; San Francisco. Abstract #OS51C-1503.

Shepherd, J.B., 1992. Comment on “Subduction and seismic hazard in the Lesser Antilles” by Pascal Bernard and Jerome Lambert, 10.

Simpkin, P.G., Davis, A., 1993. For seismic profiling in very shallow water, a novel receiver. Sea Technology 34, 21–28.

Spiske, M., Pilarczyk, J.E., Mitchell, S., Halley, R.B., Otai, T., 2021. Coastal erosion and sediment reworking caused by hurricane Irma – implications for storm impact on low-lying tropical islands. Earth Surf Processes Landf esp.5293. https://doi.org/10.1002/esp.5293

Stoddart, D.R., Bryan, G.W., Gibbs, P.E., 1973. Inland mangroves and water chemistry, Barbuda, West Indies. Journal of Natural History 7, 33–46. https://doi.org/10.1080/00222937300770031

https://doi.org/10.5194/nhess-2022-262
Preprint. Discussion started: 14 February 2023

Takagi, H., Esteban, M., Shibayama, T., Mikami, T., Matsumaru, R., De Leon, M., Thao, N. d., Oyama, T., Nakamura, R., 2017. Track analysis, simulation, and field survey of the 2013 Typhoon Haiyan storm surge. Journal of Flood Risk Management 10, 42–52. https://doi.org/10.1111/jfr3.12136

Thirumalai, K., Taylor, F.W., Shen, C.-C., Lavier, L.L., Frohlich, C., Wallace, L.M., Wu, C.-C., Sun, H., Papabatu, A.K., 2015. Variable Holocene deformation above a shallow subduction zone extremely close to the trench. Nat Commun 6, 7607. https://doi.org/10.1038/ncomms8607

Tweedy, 1981. A ~~HISTORY~~ History of ~~OF~~ B~~arbuda~~~~ARBUDA~~ ~~UNDER THE~~under the C~~odringtons~~~~ODRINGTONS~~ 1738-1833.

United Nations Development Programme, 2019. Housing Support to Barbuda (Project Document No. 00117863). United Nations Development Programme, Antigua and Barbuda.

van Rijsingen, E., Calais, E., Jolivet, R., De Chabalier, J.B., Robertson, R., Ryan, G.A., Simythe, S., 2022. Ongoing tectonic subsidence in the Lesser Antilles subduction zone. Geophysical Journal International. https://doi.org/DOI: 10.1093/gji/ggac192

Wallace, E.J., Donnelly, J.P., Hengstum, P.J., Wiman, C., Sullivan, R.M., Winkler, T.S., d'Entremont, N.E., Toomey, M., Albury, N., 2019. Intense ~~Hurricane~~ hurricane ~~Activity~~ activity ~~Over~~ over the ~~Past~~ past 1500 ~~Years~~ years at South Andros Island, The Bahamas. Paleoceanography and Paleoclimatology 34, 1761–1783. https://doi.org/10.1029/2019PA003665

Watt, S.F.L., Talling, P.J., Vardy, M.E., Heller, V., Hühnerbach, V., Urlaub, M., Sarkar, S., Masson, D.G., Henstock, T.J., Minshull, T.A., Paulatto, M., Le Friant, A., Lebas, E., Berndt, C., Crutchley, G.J., Karstens, J., Stinton, A.J., Maeno, F., 2012. Combinations of volcanic-flank and seafloor-sediment failure offshore Montserrat, and their implications for tsunami generation. Earth and Planetary Science Letters 319–320, 228–240. https://doi.org/10.1016/j.epsl.2011.11.032

Weil-Accardo, J., Feuillet, N., Philibosian, B., Guihou, A., Jacques, E., Cabioch, G., Anglade, A., Meriaux, A. -S., Deschamps, P., 2022. Interaction ~~Between~~ between ~~Climate~~ climate and ~~Tectonics~~ tectonics in the ~~Northern~~ northern Lesser Antilles ~~Inferred~~ inferred ~~From~~ from the Last Interglacial ~~Shoreline~~ shoreline on Barbuda Island. Geochem Geophys Geosyst 23. https://doi.org/10.1029/2021GC010045

Weltje, G.J., Bloemsma, M.R., Tjallingii, R., Heslop, D., Röhl, U., Croudace, I.W., 2015. Prediction of ~~G~~geochemical ~~C~~composition from XRF ~~C~~core ~~S~~scanner ~~D~~data: A ~~N~~new ~~M~~multivariate ~~A~~approach ~~I~~including ~~A~~automatic ~~S~~selection of ~~C~~calibration ~~S~~samples and ~~Q~~quantification of ~~U~~uncertainties, in: Croudace, I.W., Rothwell, R.G. (Eds.), Micro-XRF Studies of Sediment Cores, Developments in Paleoenvironmental Research. Springer Netherlands, Dordrecht, pp. 507–534. https://doi.org/10.1007/978-94-017-9849-5_21

Wigley, P., 1973. The distribution of strontium in limestones on Barbuda, West Indies. Sedimentology 20, 295–304. https://doi.org/10.1111/j.1365-3091.1973.tb02051.x

Winkler, T.S., van Hengstum, P.J., Donnelly, J.P., Wallace, E.J., D'Entremont, N., Hawkes, A.D., Maio, C.V., Sullivan, R.M., Woodruff, J.D., 2022. Oceanic passage of hurricanes across Cay Sal Bank in The Bahamas over the last 530 years. Marine Geology 443, 106653. https://doi.org/10.1016/j.margeo.2021.106653

Zahibo, N., Pelinovsky, E.N., 2001. Evaluation of tsunami risk in the Lesser Antilles. Natural Hazards and Earth System Science 1, 221–231. https://doi.org/10.5194/nhess-1-221-2001

Zahibo, N., Pelinovsky, E., Yalciner, A.C., Kurkin, A., Koselkov, A., Zaitsev, A., 2003. The 1867 Virgin Island Tsunami. Natural Hazards and Earth System Sciences 3, 367–376. https://doi.org/10.5194/nhess-3-367-2003

Zahibo, N., Pelinovsky, E., Okal, E., Yalçiner, A., Kharif, C., Talipova, T., Kozelkov, A., 2005. The earthquake and tsunami of November 21, 2004 at les Saintes, Guadeloupe, Lesser Antilles. Science of Tsunami Hazards 23, 25.

https://doi.org/10.5194/nhess-2022-262
Preprint. Discussion started: 14 February 2023

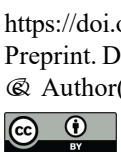

Natural Hazards and Earth System Sciences
Discussions
Open Access
EGU

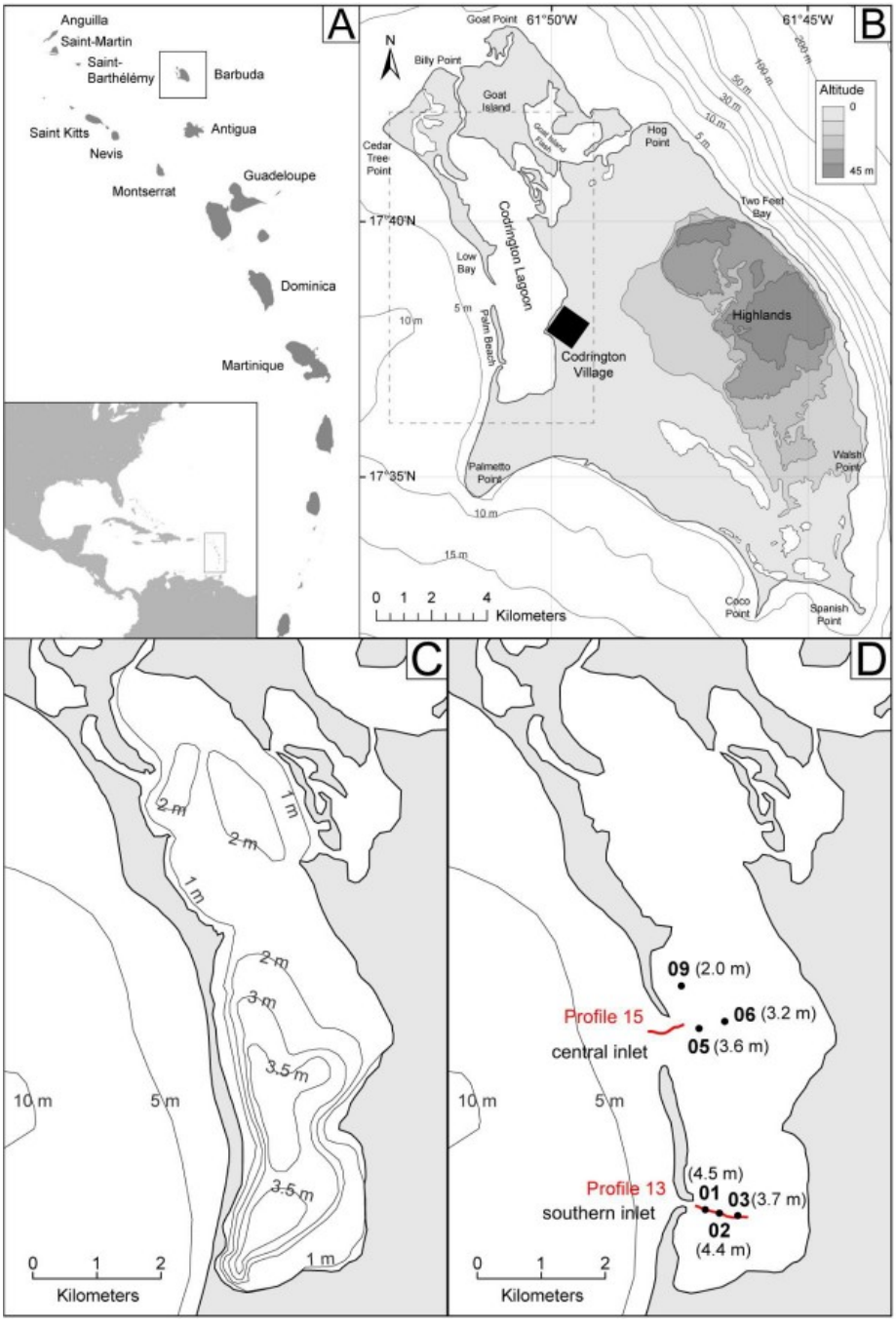

1015

Figure 1. (A) The Caribbean Sea and Lesser Antilles Arc (https://freevectormaps.com/world-maps/caribbean/WRLD-CI-01-0001?ref=atr). (B) Topography of Barbuda Island in 2018 (after Irma), modified from Bain et al., 2018 and Brasier 1975a, 1975b.

https://doi.org/10.5194/nhess-2022-262
Preprint. Discussion started: 14 February 2023

Natural Hazards and Earth System Sciences
Discussions

(C) Codrington lagoon morpho-bathymetry, from Brasier 1975a, 1975b. (D) Codrington lagoon morphology 3 months after Hurricane Irma from a satellite image of Barbuda obtained in December 2018 (Google Earth Pro V 7.3.4.8248. December 2018. Barbuda, 17°38'46.87''N, 61°50'48.67''W, Eye alt 30 kilometers. Landsat/Copernicus [December 10, 2021]). The black dots correspond to sedimentary core locations sampled in March 2018 with their respective water depths. The two red lines correspond to seismic profiles recorded in June 2021.

Year	Name	Month	Hurricane category (SSHWS) within 30 km around Codrington Lagoon	Distance hurricane-Codrington Lagoon (km)	Hurricane path with respect to Barbuda Island	Mean wind speed (kt)	Pressure (mb)
2017	Irma	August	5	< 1	On the island (N)	155	914
2000	Debby	August	1	6	SW	65	993
1996	Bertha	July	1	10	SW	75	985
1995	Luis	August	4	< 1	On the island (SW)	115	945
1990	Klaus	October	1	23	NE	65	992
1960	Donna	August-September	3	1	On the island (NE)	110	956
1950	Dog	August-September	4	27	SW	115	NA
1932	Unnamed	September-October	3	24	SW	105	NA
1922	Unnamed	September	3	4	SW	100	NA
1906	Unnamed	August-September	2	8	NE	90	NA
1876	Unnamed	September	2	30	N	90	NA
1871	Unnamed	September-October	1	15	NE	75	NA
1859	Unnamed	September	1	13	S	70	NA

Table 1. Hurricanes that passed within 30 km from Codrington lagoon (Barbuda) from 1859 to 2017 (NOAA, 2021, Historical Hurricane Tracks). SSHWS: Saffir–Simpson Hurricane Wind Scale. Kt: knot, mb: millibar.

https://doi.org/10.5194/nhess-2022-262
Preprint. Discussion started: 14 February 2023

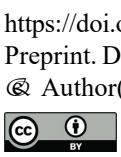

Natural Hazards and Earth System Sciences
Discussions
Open Access
EGU

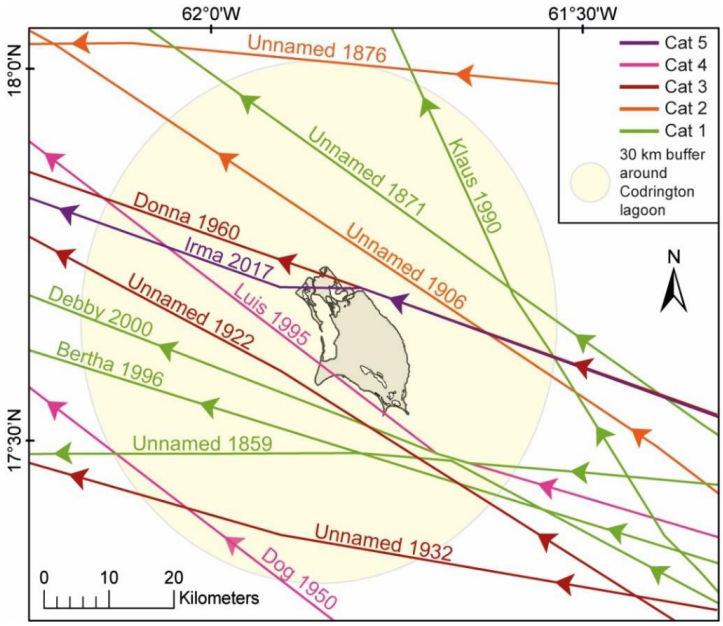

Figure 2. Historical hurricane tracks (1859–2017) passing within 30 km from Codrington Lagoon (Barbuda) (NOAA, 2021, Historical Hurricane Tracks).

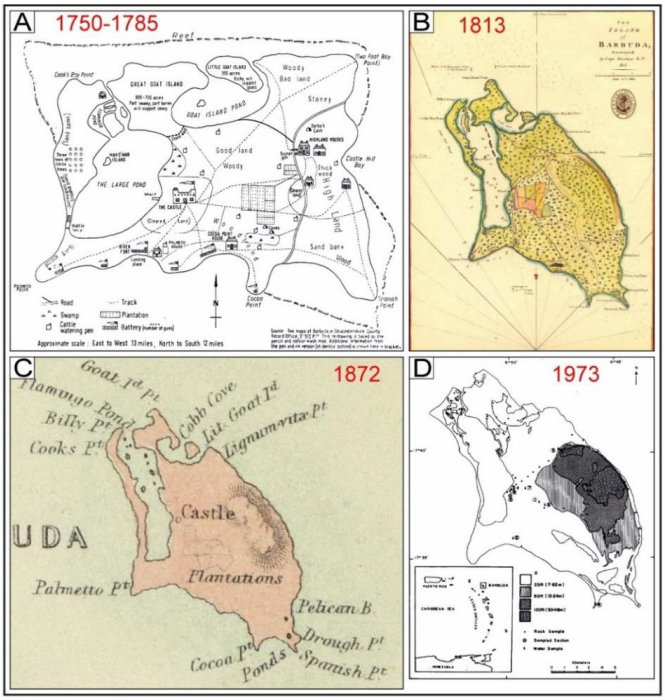

https://doi.org/10.5194/nhess-2022-262
Preprint. Discussion started: 14 February 2023

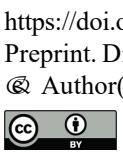

Natural Hazards and Earth System Sciences
Discussions
Open Access
EGU

Figure 3. Barbuda old nautical maps. (A) Two maps of Barbuda, in Gloucestershire County. Record Office D1610 P17. This redrawing is based on the pencil and color-wash map. Additional information from the pen and ink version (of identical outline) is shown here in brackets, from Tweedy, 1981; (B) The Island of Barbuda, surveyed in 1813 by Capt. Deckar, R. N., Hydrographical Office (PRO, CO 700, MP/8 Antigua X/04800), from Bain et al., 2018; (C) The West Indies. By G.H. Swanston, Edinr. (with) The Most Important Of The Lesser British Islands On An Enlarged Scale. LXI. Engd. by G.H. Swanston Edinburgh. A. Fullarton & Co. Edinburgh, London & Dublin, from David Rumsey Map Collection (davidrumsey.com); (D) Barbuda; location and elevation map, from Wigley, 1973.

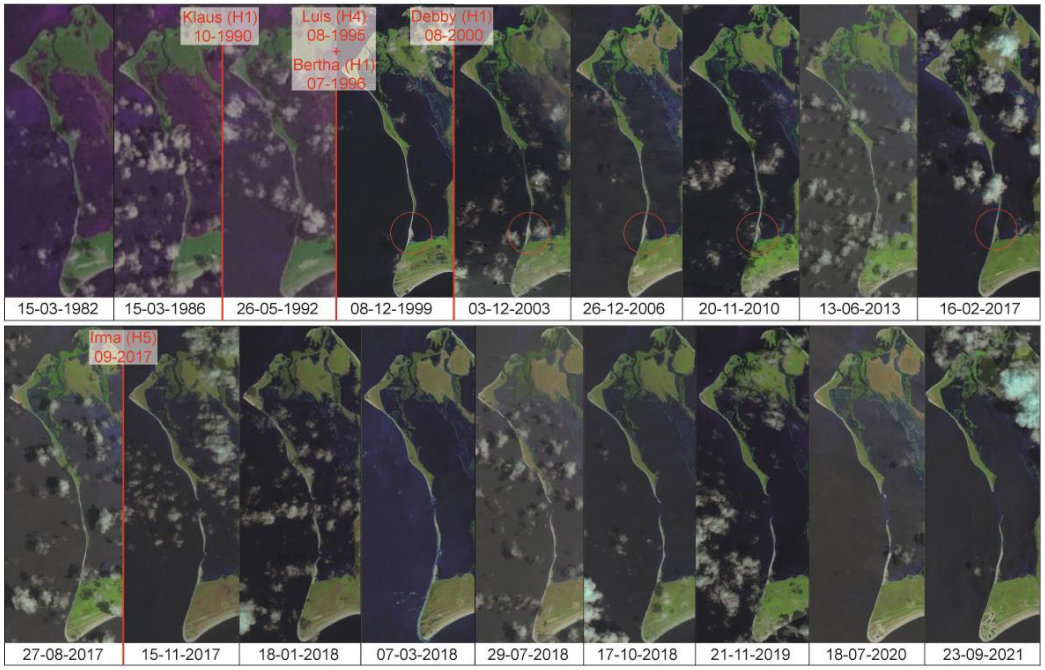

Figure 4. Satellite images displaying morphological evolutions of the Codrington Lagoon western sandy barrier over the period 1982–2021 (Landsat and Global Land Survey data sets). The images in chronological order are (from glovis.usgs.gov): Landsat 1-5 MSS C1 Level-1 LM03_L1GS_002048_19820315_20180413_01_T2; Landsat 1-5 MSS C1 Level-1 LM05_L1GS_002048_19860315_20180331_01_T2; Landsat 1-5 MSS C1 Level-1 LM04_L1TP_002048_19920526_20180318_01_T2; Global Land Survey P002R048_7X19991208; Global Land Survey LE70020482003337EDC03; Global Land Survey LE70020482006057EDC00; Global Land Survey LE70020482010324ASN00; Landsat 8 OLI/TIRS C1 Level-1 LC08_L1TP_002048_20130613_20170504_01_T1; Landsat 8 OLI/TIRS C1 Level-1 LC08_L1TP_002048_20170216_20170228_01_T1; Landsat 8 OLI/TIRS C1 Level-1 LC08_L1TP_002048_20170827_20170914_01_T1; Landsat 8 OLI/TIRS C1 Level-1 LC08_L1TP_002048_20171115_20171122_01_T1; Landsat 8 OLI/TIRS C1 Level-1 LC08_L1TP_002048_20180118_20180206_01_T1; Landsat 8 OLI/TIRS C1 Level-1 LC08_L1TP_002048_20180307_20180320_01_T1; Landsat 8 OLI/TIRS C1 Level-1 LC08_L1TP_002048_20180729_20180814_01_T1; Landsat 8 OLI/TIRS C1 Level-1 LC08_L1TP_002048_20181017_20181030_01_T1; Landsat 8 OLI/TIRS C1 Level-1

https://doi.org/10.5194/nhess-2022-262
Preprint. Discussion started: 14 February 2023

Natural Hazards and Earth System Sciences
Discussions
Open Access
EGU

LC08_L1TP_002048_20191121_20191203_01_T1;	**Landsat**	**8**	**OLI/TIRS**	**C1**	**Level-1**
LC08_L1TP_002048_20200718_20200722_01_T1;	**Landsat**	**8**	**OLI/TIRS**	**C1**	**Level-1**

LC08_L1TP_002048_20210923_20210923_01_RT. The red bars correspond to hurricanes that passed within 30 km from Codrington Lagoon during the visualized period. H1, H2, and H5 indicate the hurricane category on the Saffir–Simpson hurricane wind scale.

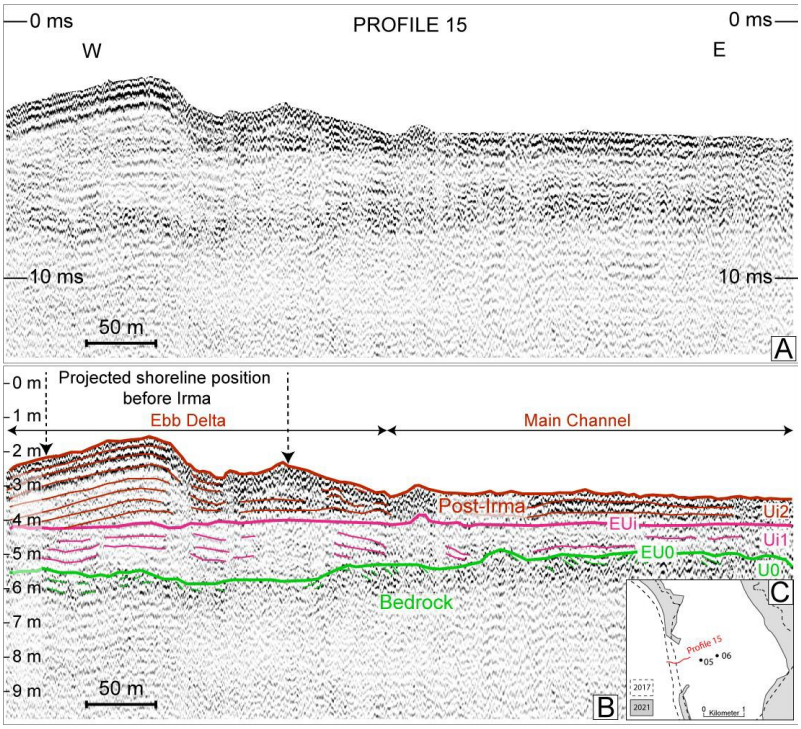

Figure 5. (A) Seismic profile 15 (length approximately 570 m) showing a part of the lagoon central inlet structure (east–west transect) in June 2021. (B) Interpreted profile. (C) Profile localization in comparison with the sandy barrier in 2021 (in gray) and in 2017 before Hurricane Irma (in dotted lines).

https://doi.org/10.5194/nhess-2022-262
Preprint. Discussion started: 14 February 2023

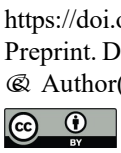

Natural Hazards and Earth System Sciences
Discussions

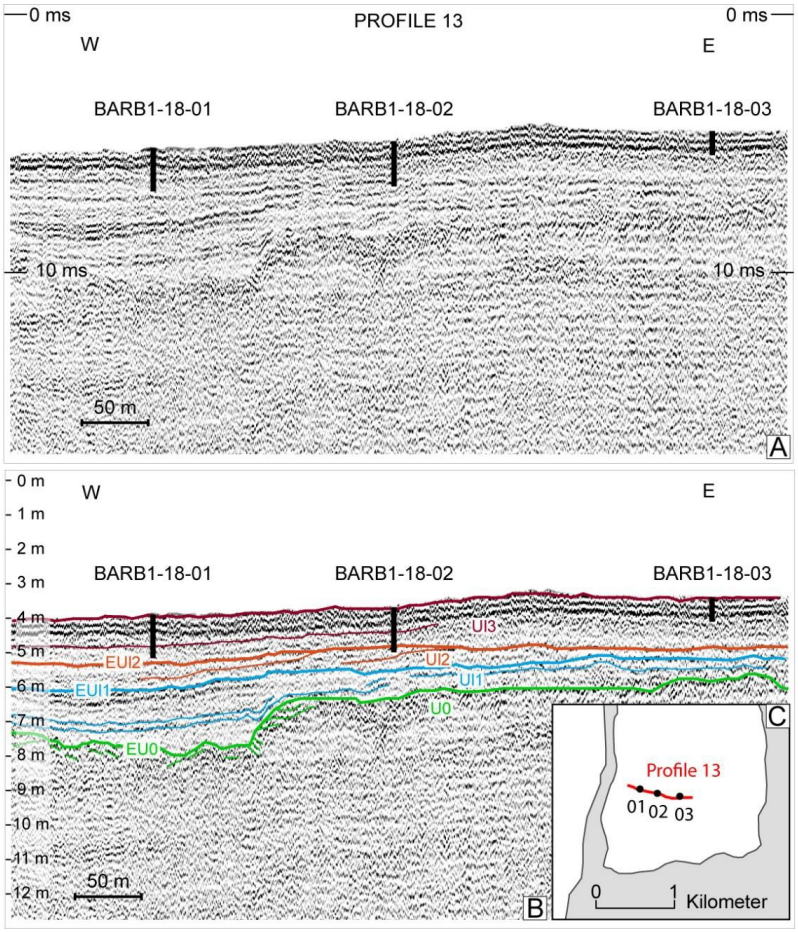

Figure 6. (A) Seismic profile 13 (length approximately 750 m) showing the south lagoon infill structure along an east–west transect in June 2021. (B) Interpreted profile. (C) Profile localization in comparison with the sandy barrier in 2021.

https://doi.org/10.5194/nhess-2022-262
Preprint. Discussion started: 14 February 2023

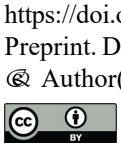

Natural Hazards and Earth System Sciences
Discussions
Open Access
EGU

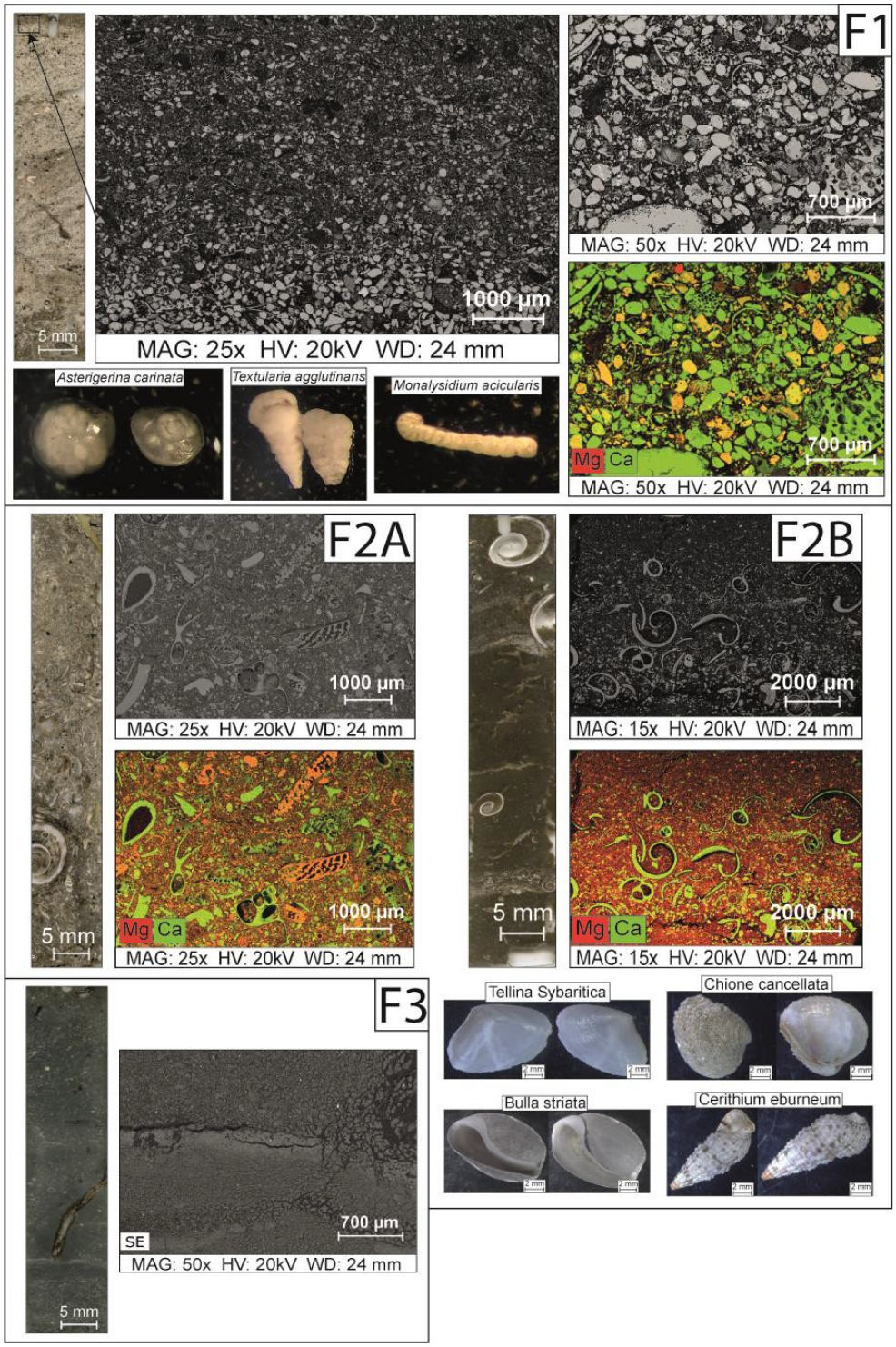

https://doi.org/10.5194/nhess-2022-262
Preprint. Discussion started: 14 February 2023

Natural Hazards and Earth System Sciences
Discussions

Figure 7. Main facies of the six cores from Codrington Lagoon. For every facies (F1, F2A, F2B and F3), there is a picture of a thin slide on the left, SEM images, and geochemical cartographies (with Ca in green, Mg in red) from cores BARB1-18-01 and BARB1-18-05. In F1 and F F2, there are optical microscope photographs of foraminifera (<125 µm) and bivalves and gastropods shells, respectively, taken from cores BARB1-18-01 and BARB1-18-05.

https://doi.org/10.5194/nhess-2022-262
Preprint. Discussion started: 14 February 2023

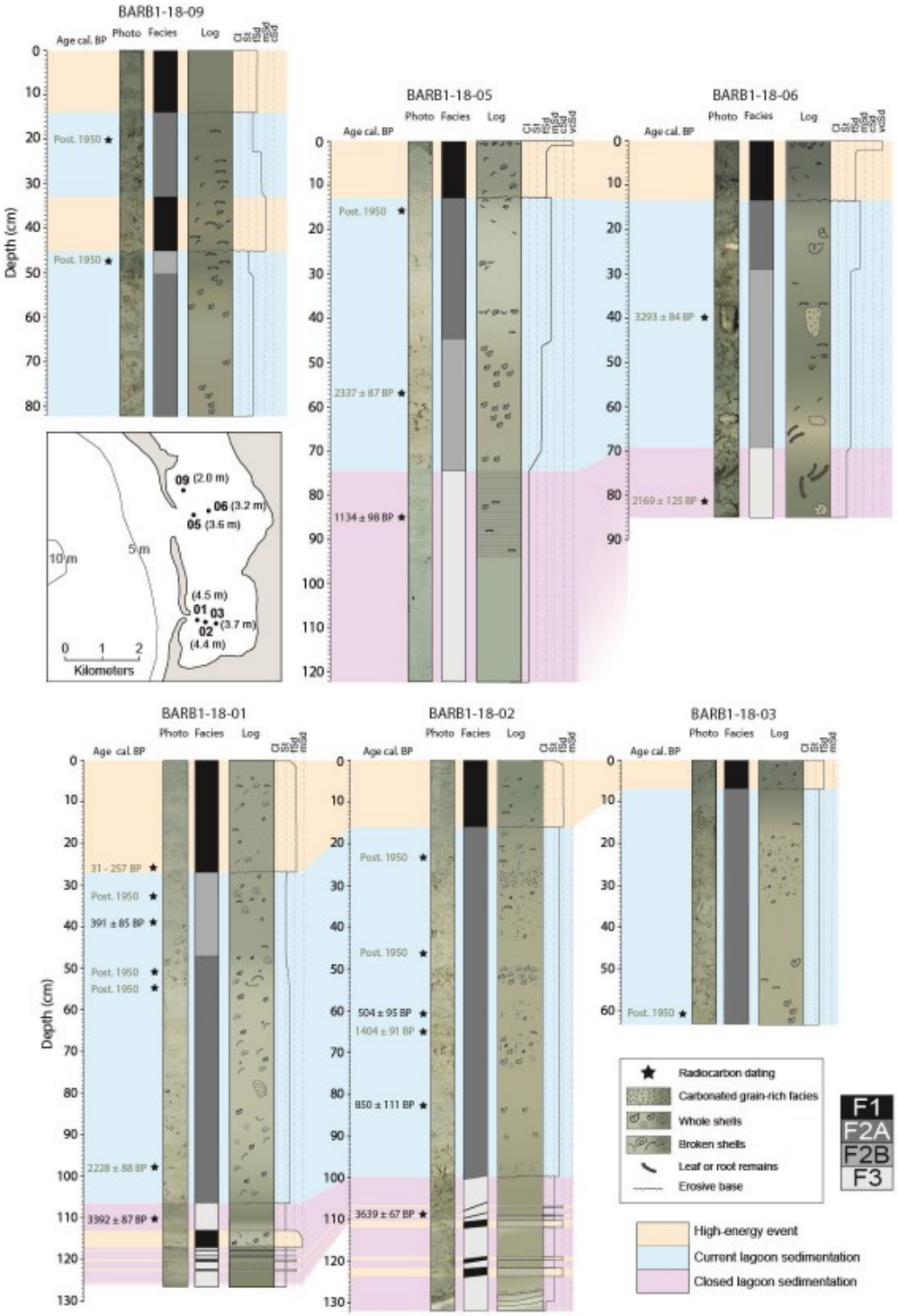

https://doi.org/10.5194/nhess-2022-262
Preprint. Discussion started: 14 February 2023

Natural Hazards and Earth System Sciences
Discussions

Figure 8. Photos, facies logs, and sedimentary logs for cores BARB-18-01, 02, 03, 05, 06 and 09 with the depth of the ^{14}C ages in cal. BP (indicated with black stars). The most reliable ^{14}C ages are written in black, and the others are shown in gray. The orange, blue and violet lines highlight the different types of sedimentary deposits that were correlated between cores. The indicated depths are relative to the bottom of the lagoon. The coringes locations and water depths are indicated on the map.

https://doi.org/10.5194/nhess-2022-262
Preprint. Discussion started: 14 February 2023

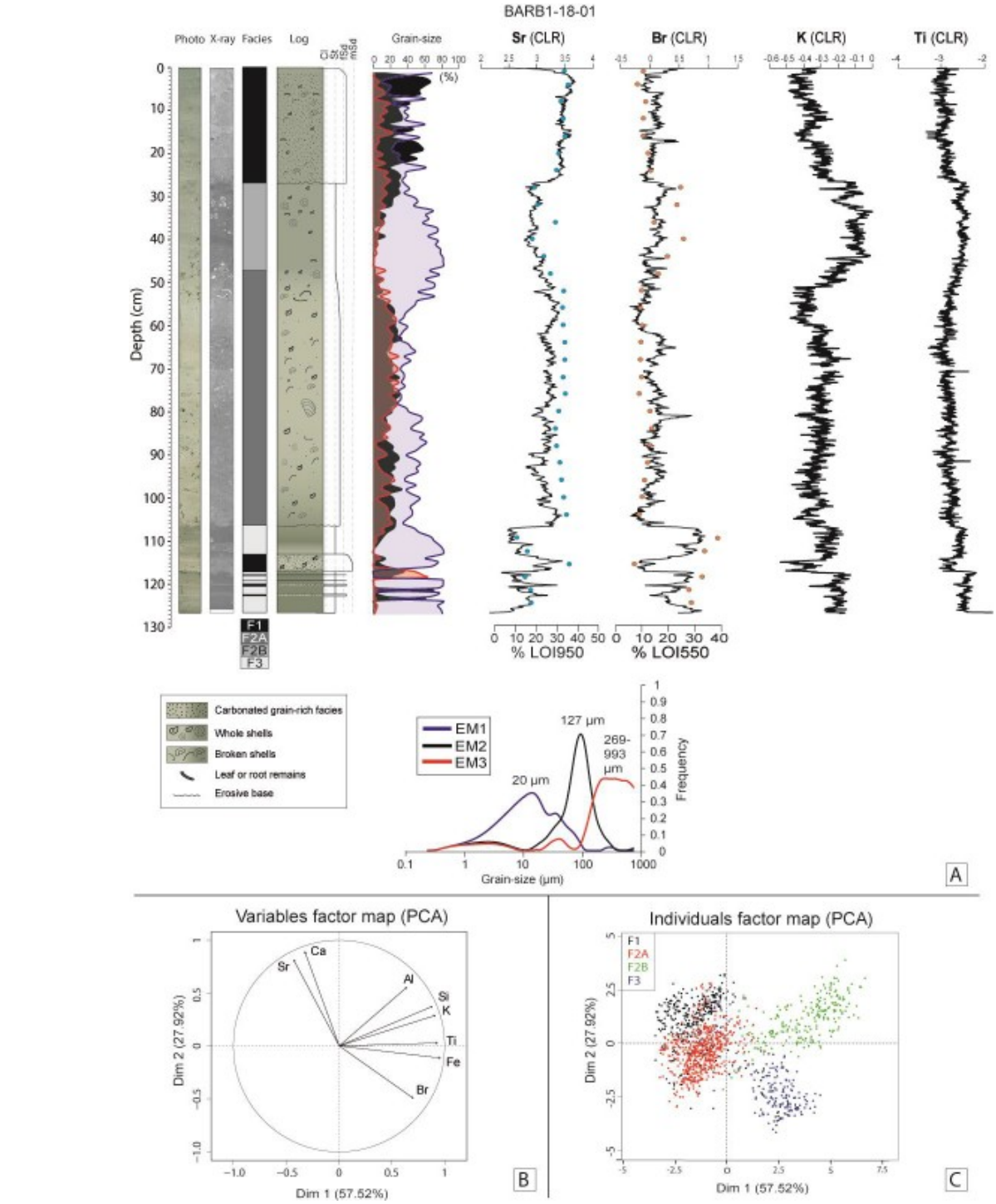

1085

https://doi.org/10.5194/nhess-2022-262
Preprint. Discussion started: 14 February 2023

Natural Hazards and Earth System Sciences
Discussions

Figure 9. Geochemical and grain-size data for core BARB1-18-01. (A) From left to right, picture, X-ray, facies log, lithological description, grain-size endmember distributions and their corresponding grain-size modes underneath, centered log-ratio (CLR) XRF data for Sr, Br, K and Ti. The LOI950 and LOI550 percentages are superimposed on the Sr and Br data, respectively. (B) PCA of the XRF data with the grain-size endmembers. (C) Map of the geochemical data distribution with facies information. The black dots correspond to F1, the red dots to F2A, the green dots to F2B and the blue dots to F3.

https://doi.org/10.5194/nhess-2022-262
Preprint. Discussion started: 14 February 2023

Natural Hazards and Earth System Sciences
Discussions

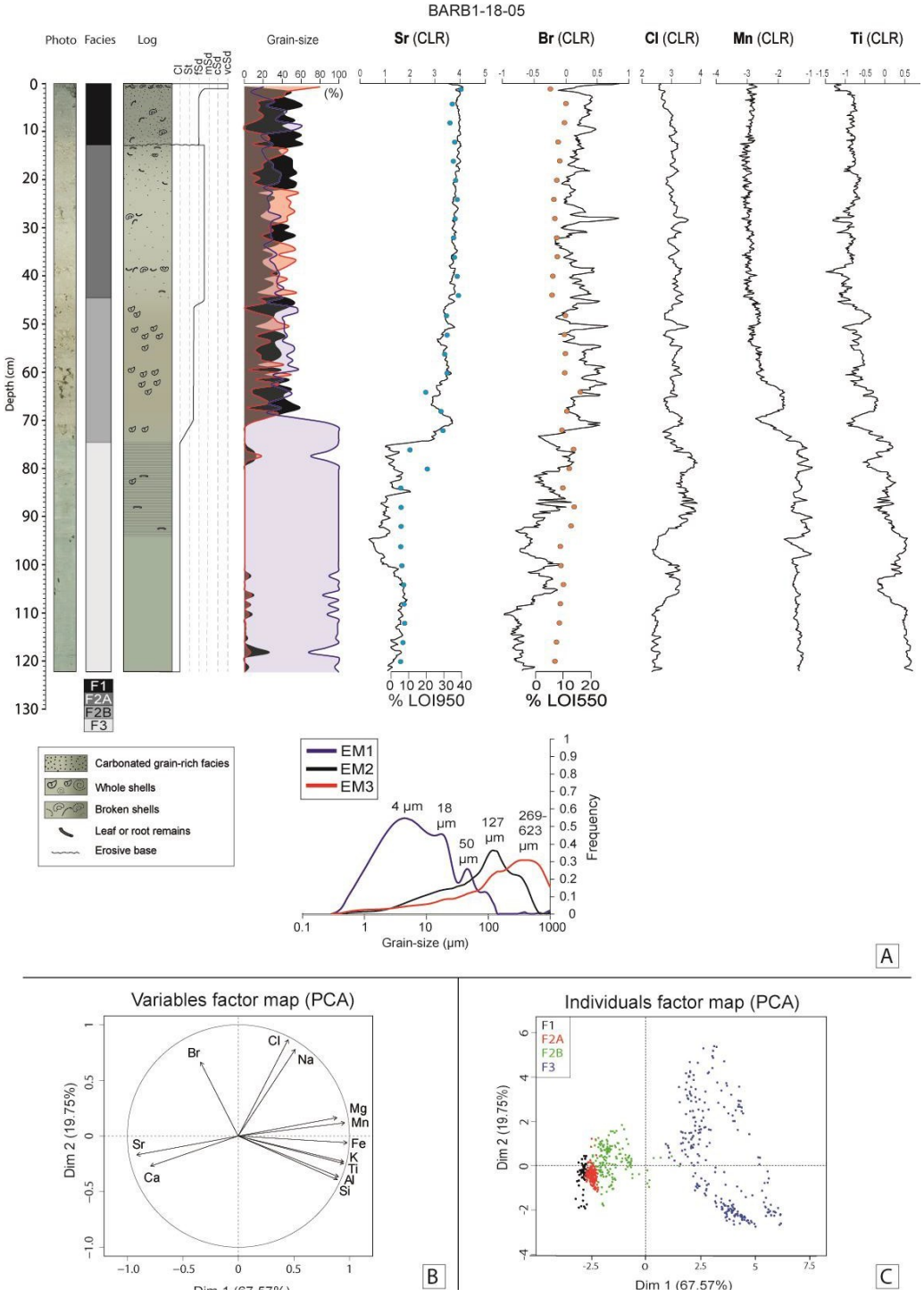

1095

https://doi.org/10.5194/nhess-2022-262
Preprint. Discussion started: 14 February 2023

Figure 10. Geochemical and grain-size data for core BARB1-18-05. (A) From left to right, picture, X-ray, facies log, lithological description, grain-size endmember distributions and their corresponding grain-size modes underneath, centered log-ratio (CLR) XRF data for Sr, Br, Cl, Mn and Ti. The LOI950 and LOI550 percentages are superimposed on the Sr and Br data, respectively. (B) PCA of the XRF data with the grain-size endmembers. (C) Map of the geochemical data distribution with facies information. The black dots correspond to F1, the red dots to F2A, the green dots to F2B and the blue dots to F3.

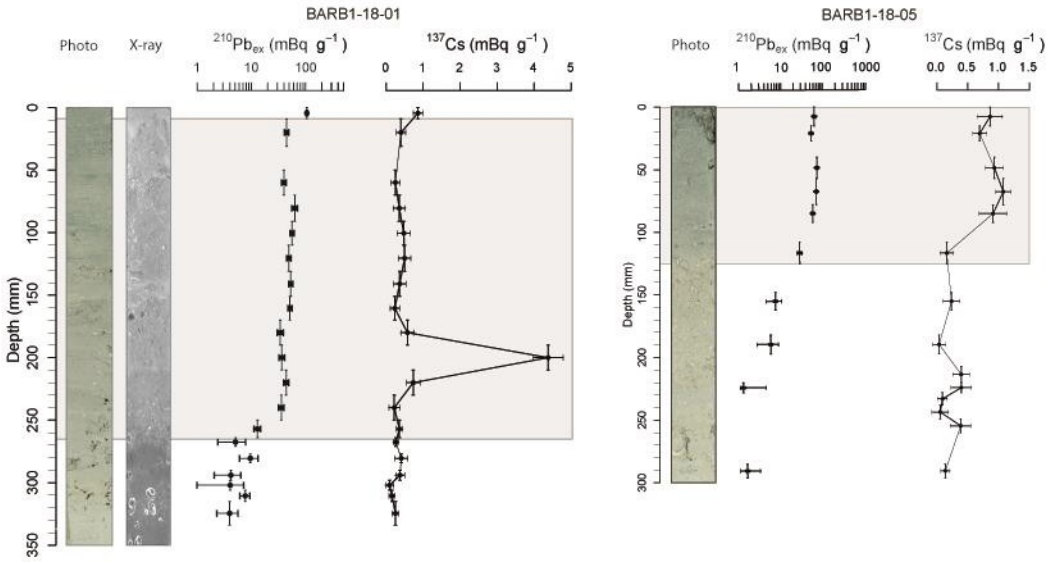

Figure 11. BARB1-18-01 and BARB1-18-05 short-lived radionuclide data with ^{210}Pbex on a logarithmic scale associated with the ^{137}Cs activity profiles, core pictures and X-ray. The gray rectangles display the F1 layer boundaries.

Sample name	Core	Depth (cm)	Sample type	Age (BP)	Calibrated age range at 95% confidence interval (cal. BP)
SacA54670	BARB1-18-01	26.5	Plant macroremains	65 ± 30	33 - 257
Poz-118677	BARB1-18-01	34.5	Plant macroremains	Post. 1950	-
SacA57046	BARB1-18-01	40	Plant macroremains	340 ± 30	311 - 480
SacA54671	BARB1-18-01	52	Plant macroremains	Post. 1950	-
Poz-118678	BARB1-18-01	56	Plant macroremains	Post. 1950	-
SacA57047	BARB1-18-01	101	Plant macroremains	2225 ± 30	2153 - 2328
SacA57048	BARB1-18-01	113.5	Plant macroremains	3165 ± 30	3277 -3451
SacA54673	BARB1-18-02	23	Plant macroremains	Post. 1950	-
SacA57049	BARB1-18-02	46	Plant macroremains	Post. 1950	-
Poz-118675	BARB1-18-02	60.5	Plant macroremains	440 ± 30	342 -532
SacA54674	BARB1-18-02	65	Plant macroremains	1520 ± 30	1341 - 1522
SacA57050	BARB1-18-02	82.5	Plant macroremains	940 ± 60	734 - 955
SacA54675	BARB1-18-02	108.5	Plant macroremains	3395 ± 30	3570 - 3704

https://doi.org/10.5194/nhess-2022-262
Preprint. Discussion started: 14 February 2023

Natural Hazards and Earth System Sciences
Discussions
Open Access
EGU

SacA57051	BARB1-18-03	60	Plant macroremains	Post. 1950	-
SacA57053	BARB1-18-05	16	Plant macroremains	Post. 1950	-
Poz-118681	BARB1-18-05	57	Plant macroremains	2310 ± 30	2185 - 2359
SacA57054	BARB1-18-05	85	Plant macroremains	1210 ± 30	1059 - 1255
Poz-113762	BARB1-18-06	39.5	Plant macroremains	3085 ± 35	3210 - 3378
SacA57055	BARB1-18-06	81	Plant macroremains	2160 ± 30	2057 - 2306
SacA57056	BARB1-18-09	20	Plant macroremains	Post. 1950	-
SacA57057	BARB1-18-09	47.5	Plant macroremains	Post. 1950	-

Table 2. ^{14}C ages for cores BARB1-18-01, BARB1-18-02, BARB1-18-03, BARB1-18-05, BARB1-18-06 and BARB1-18-09 (plant macroremains: wood, leaves and roots).